

Cite this: *Chem. Sci.*, 2024, 15, 14081

## Recent advances of metal active sites in photocatalytic CO<sub>2</sub> reduction

Wa Gao,<sup>a</sup> Haonan Li,<sup>a</sup> Jianqiang Hu,<sup>b</sup> Yong Yang,<sup>c</sup> Yujie Xiong,<sup>d</sup> Jinhua Ye,<sup>e</sup> Zhigang Zou<sup>cd</sup> and Yong Zhou<sup>bc</sup>

Photocatalytic CO<sub>2</sub> reduction captures solar energy to convert CO<sub>2</sub> into hydrocarbon fuels, thus shifting the dependence on rapidly depleting fossil fuels. Among the various proposed photocatalysts, systems containing metal active sites (MASs) possess obvious advantages, such as effective photogenerated carrier separation, suitable adsorption and activation of intermediates, and achievable C–C coupling to generate multi-carbon (C<sub>2+</sub>) products. The present review aims to summarize the typical photocatalytic materials with MAS, highlighting the critical role of different formulations of MAS in CO<sub>2</sub> photoreduction, especially for C<sub>2+</sub> product generation. State-of-the-art progress in the characterization and theoretical calculations for MAS-containing photocatalysts is also emphasized. Finally, the challenges and prospects of catalytic systems involving MAS for solar-driven CO<sub>2</sub> conversion are outlined, providing inspiration for the future design of materials for efficient photocatalytic energy conversion.

Received 25th March 2024  
Accepted 22nd July 2024

DOI: 10.1039/d4sc01978d

rsc.li/chemical-science

### 1 Introduction

Over-reliance on fossil fuels as energy carriers leads to excessive CO<sub>2</sub> emissions from combustion, which in turn causes climate change, environmental damage and energy crisis.<sup>1–3</sup> Shifting from fossil fuels to renewable energy sources to achieve carbon neutrality is an important step towards sustainable development. Therefore, there is an urgent need to find a suitable, effective, and green strategy to facilitate the conversion of CO<sub>2</sub> and access renewable energy through sustained technological innovation.

CO<sub>2</sub> capture and conversion by artificial photosynthesis can simultaneously address the rising global CO<sub>2</sub> emissions and produce hydrocarbon fuels to accomplish carbon neutrality.<sup>4–6</sup>

It is proving to be an elegant and promising solution, attracting the interest of scientists and making great strides in the efficiency of CO<sub>2</sub> conversion.<sup>7–11</sup> Specifically, the photocatalytic reduction of CO<sub>2</sub> achieves a sustainable alternative to conventional fossil fuels, which is carried out in relatively mild conditions-room temperature and pressure, driving the conversion of CO<sub>2</sub> to hydrocarbons directly without additional energy supply or harmful substance release. Photocatalytic CO<sub>2</sub> reduction consists of three main processes:<sup>12</sup> the catalyst generates electron–hole pairs under sunlight;<sup>13–15</sup> carriers separate and migrate to the surface;<sup>16</sup> CO<sub>2</sub> is activated and converted at the surface active sites, involving C–O bond breaking, C–H bond formation, and C–C coupling.<sup>17,18</sup> In fact, the CO<sub>2</sub> molecule possesses a rather stable structure with high dissociation energy to cleave the C=O bond (750 kJ mol<sup>−1</sup>), which poses a challenge for the activation and conversion of CO<sub>2</sub>.<sup>19</sup> In addition, solar-driven CO<sub>2</sub> reduction involves complex multi-step conversions that, depending on the number of electrons and protons transferred, produces CO,<sup>20–22</sup> CH<sub>3</sub>OH,<sup>23–25</sup> CH<sub>4</sub>,<sup>26,27</sup> C<sub>2</sub>H<sub>4</sub>,<sup>28–30</sup> C<sub>2</sub>H<sub>6</sub>,<sup>31,32</sup> C<sub>2</sub>H<sub>5</sub>OH,<sup>33</sup> etc. Due to the diversity of products of CO<sub>2</sub> photoreduction, achieving highly selective CO<sub>2</sub> conversion to generate specific target products is extremely challenging.

Various strategies have been employed to improve the efficiency and selectivity of CO<sub>2</sub> photoreduction, including enhancing light absorption,<sup>34,35</sup> promoting carrier separation,<sup>36</sup> constructing active sites,<sup>37</sup> and promoting C–C coupling.<sup>38</sup> According to the current findings, MAS possesses significant advantages in improving the performance of photocatalytic reduction of CO<sub>2</sub> and promoting C–C coupling to obtain C<sub>2+</sub> products.<sup>39–41</sup> This review mainly introduces the research

<sup>a</sup>School of Physical Science and Technology, Tiangong University, Tianjin 300387, P. R. China<sup>b</sup>School of Chemical and Environmental Engineering, Anhui Polytechnic University, Wuhu 241000, P. R. China<sup>c</sup>School of Physics, Jiangsu Key Laboratory of Nanotechnology, Eco-materials and Renewable Energy Research Center (ERERC), National Laboratory of Solid State Microstructures, Collaborative Innovation Center of Advanced Microstructures, Nanjing University, Nanjing 210093, P. R. China<sup>d</sup>School of Science and Engineering, The Chinese University of Hongkong (Shenzhen), Shenzhen, Guangdong 518172, P. R. China<sup>e</sup>Key Laboratory of Soft Chemistry and Functional Materials (MOE), Nanjing University of Science and Technology, Nanjing 210094, P. R. China<sup>f</sup>Jiangxi Normal Univ., Inst. Adv. Mat. IAM, Coll. Chem. & Chem. Engn., Nanchang 330022, P. R. China<sup>g</sup>National Institute for Materials Science (NIMS), International Center Materials Nanoarchitecture MANA, 1-1 Namiki, Tsukuba, Ibaraki 305-0044, Japan<sup>h</sup>School of Chemistry and Materials Science, University of Science and Technology of China, Hefei 230036, Anhui, P. R. China

progress of MAS in driving photocatalytic CO<sub>2</sub> conversion (Fig. 1). Photocatalytic systems containing MAS including metal oxides, metal sulfides, layered double hydroxides (LDHs), metal organic framework (MOF), covalent organic frameworks (COF), single atom catalysts, and metal complexes are summarized. The achievement of MAS with different formulations in photocatalytic CO<sub>2</sub> conversion is systemically explored while mechanisms that drive performance improvement are discussed in detail. The development of characterization techniques and theoretical calculation to determine the structure and function of MAS in CO<sub>2</sub> photoreduction is also highlighted. Finally, the difficulties, challenges, and novel viewpoints of feasible solutions are addressed regarding the design of advanced photocatalysts containing MAS for efficient solar energy conversion.

## 2 Photocatalytic systems with MAS

Micro-nanostructures containing MAS, including metal oxides, metal sulfides, LDHs, MOF, COF, single atom catalysts, and metal complexes are widely used in photocatalytic CO<sub>2</sub> reduction. According to the process and mechanism of CO<sub>2</sub> photoreduction, the catalytic systems with high light absorption capacity, sufficient carrier separation, and abundant active sites show obvious advantages in the yield and selectivity of CO<sub>2</sub> conversion.

### 2.1 Metal oxides

In the complex and diverse photocatalytic systems, metal oxides have become the most representative and well-established photocatalysts. A large number of strategies aimed at modulating the band gap, facilitating carrier separation, and establishing active sites have been proposed and intensively investigated in metal oxides.<sup>42–44</sup> TiO<sub>2</sub>, as a representative metal oxide, has become a photocatalyst of wide interest due to its low toxicity, high stability and economic advantages. Defect engineering, heterostructure construction, heteroatom doping, and surface modulation have been proposed to regulate the carrier

migration, CO<sub>2</sub> adsorption and activation of TiO<sub>2</sub>-based catalysts. The synergistic effect of Ru and oxygen vacancies (Vo) on the photocatalytic performance of TiO<sub>2</sub> (Ru-TiO<sub>2-x</sub>) was systematically investigated.<sup>45</sup> It was found that Ru-TiO<sub>2-x</sub> exhibited high activity for the photoreduction of CO<sub>2</sub> to CH<sub>4</sub>. The introduced Vo in Ru-TiO<sub>2-x</sub> provided important contributions to promote photogenerated carrier separation and facilitate CO<sub>2</sub> conversion. The Ru species effectively captured photogenerated electrons, which inhibited further photogenerated carrier recombination.

Photocatalytic CO<sub>2</sub> reduction for the generation of C<sub>2+</sub> products was achieved in metal-oxide systems. The vacancy-rich TiO<sub>2</sub> with Cu single atoms loading produced C<sub>3</sub>H<sub>8</sub>, which involved an overall 20 e<sup>-</sup> reduction and two sequential C-C coupling processes.<sup>46</sup> The Cu-Ti-V<sub>O</sub> unit in the Ti<sub>0.91</sub>O<sub>2</sub> matrix was formed through the modulation of the electronic coupling interaction between the Cu atoms and adjacent Ti atoms by Vo. This unique unit lowered the energy levels of the key \*CHOCO and \*CH<sub>2</sub>OCOCO intermediates, thereby tuning the C<sub>1</sub>-C<sub>1</sub> and C<sub>1</sub>-C<sub>2</sub> couplings to thermodynamically favourable exothermic processes (Fig. 2a). Moreover, the metastable hexagonal WO<sub>3</sub> (h-WO<sub>3</sub>), offering a suitable bandgap, exhibited efficient photoreduction of CO<sub>2</sub> to C<sub>2</sub>H<sub>4</sub>.<sup>47</sup> The blue color of the metastable state of WO<sub>3</sub> was attributed to the reduction of W<sup>6+</sup> to W<sup>5+</sup> or W<sup>4+</sup> with the increase of the reduced state, which indicated the existence of Vo. The surface Vo enhanced the light absorption capability and promoted the photogenerated carrier separation. More importantly, the W-S-W sites formed by the S atom,

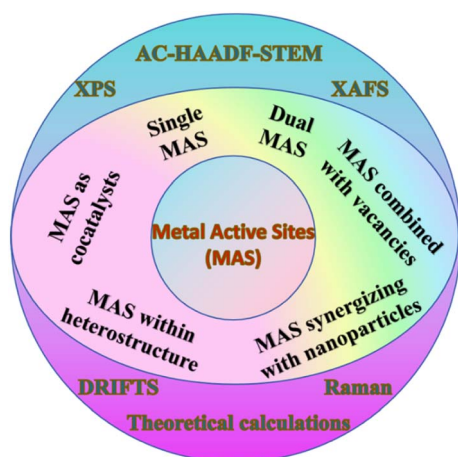


Fig. 1 Overview of the metal active sites in photocatalytic CO<sub>2</sub> reductions.

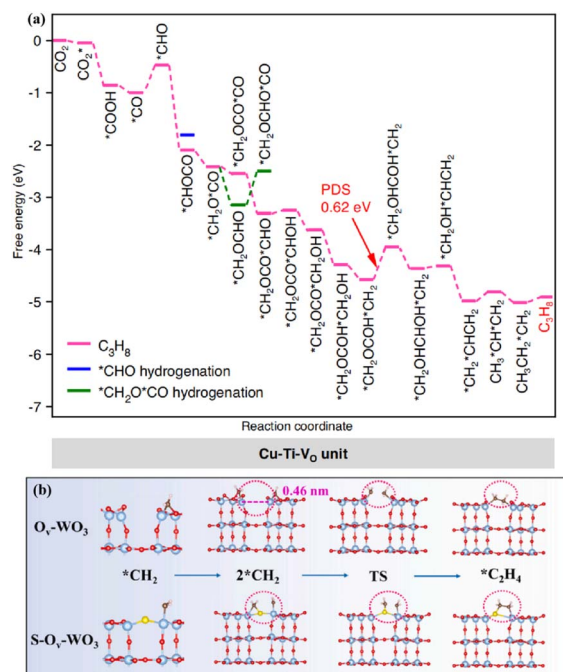


Fig. 2 (a) Gibbs free energy diagrams of CO<sub>2</sub> reduction on the Cu-Ti-V<sub>O</sub> unit. This figure has been reproduced from ref. 46 with permission from Springer Nature, copyright 2023. (b) The C-C coupling process of Ov-WO<sub>3</sub> and S-Ov-WO<sub>3</sub>. This figure has been reproduced from ref. 47 with permission from Elsevier, copyright 2023.



which replaced oxygen atoms and bridged the adjacent W atoms, benefited the adsorption of  $^*\text{CH}_2$  intermediates and promoted the C–C coupling to generate  $\text{C}_2\text{H}_4$  (Fig. 2b).

Based on the above analysis, the MAS constructed in the metal oxide system is structurally stable, successfully achieving efficient photocatalytic  $\text{CO}_2$  conversion with  $\text{C}_{2+}$  generation. In fact, MAS in metal oxides often synergizes with defect and doping atoms to achieve performance enhancement. Therefore, MAS introduced in metal oxides usually needs multi-step experimental treatment processes.

## 2.2 Transition metal sulfides/phosphorus sulfides

Various metal chalcogenides, such as ZnS, CdS, MnS, CdSe,  $\text{ZnIn}_2\text{S}_4$  (ZIS), and  $\text{CuIn}_5\text{S}_8$ , have exhibited progressive photocatalytic performances. Their excellent properties, including their low cost, wide range of light absorption, and high carrier mobility, have made them one of the most promising materials for  $\text{CO}_2$  conversion.

The reduction potential of ZnS is  $-1.04$  V vs. NHE, which is relatively negative and particularly suitable for the photocatalytic reduction reaction.<sup>48</sup> However, the wide band gap (3.6–3.8 eV), fast recombination of the charge carriers, and low selectivity toward  $\text{CO}_2$  reduction competing with the hydrogen evolution reaction (HER) limit the efficiency of ZnS. Cu-doped ZnS, containing abundant sphalerite and wurtzite phase (S–W) junctions, enhanced the photocatalytic activity with high CO selectivity.<sup>49</sup> The S–W phase junction containing abundant sulfur vacancies ( $\text{V}_\text{S}$ ) effectively facilitated the separation of charge carriers and the localization of photoelectrons for surface catalysis. The addition of Cu increased the electron density at the Fermi energy level, promoted the reactivity of the Cu sites, and enhanced the bonding of the catalyst surface to the  $^*\text{CO}$  intermediate, thereby improving the CO selectivity. Furthermore, the dual functional ZnS coupled with  $\text{g-C}_3\text{N}_4$  simultaneously enhanced the surface and bulk carrier separation of  $\text{g-C}_3\text{N}_4$  for the highly selective reduction of  $\text{CO}_2$  to  $\text{CH}_4$ .<sup>50</sup> ZnS acted as a cocatalyst to capture the photogenerated electrons of  $\text{g-C}_3\text{N}_4$ . It contributed a polarization electric field, which was created inside the ZnS nanoparticle along the direction of spontaneous polarization, to prompt the migration and separation of photogenerated charges from bulk to surface.

ZIS, belonging to the  $\text{AB}_2\text{X}_4$  group of ternary compounds, has been used in photocatalysis with visible light absorption.<sup>53</sup> The metallic  $\text{ZnIn}_2\text{S}_4$ , which is rich in indium vacancies ( $\text{V}_\text{In}$ ), exhibited full-spectrum responsiveness for high  $\text{CO}_2$  photoreduction efficiency.<sup>51</sup> The  $\text{V}_\text{In}$  defect state captured the excited hole ( $\text{h}^+$ ) and increased the minority carrier diffusion length, resulting in a large number of carriers moving to the surface and participating in the conversion of  $\text{CO}_2$ . Theoretical calculations revealed that  $\text{V}_\text{In}$  lowered the energy barrier of the rate-limiting step (the formation of  $\text{COOH}^*$ , Fig. 3a and b), leading to the high rate of CO evolution. In addition, anchoring single Au atoms to ultrathin ZIS ( $\text{Au}_1/\text{ZIS}$ ) nanosheets with  $\text{V}_\text{S}$  resulted in the  $\text{Au}_1\text{-S}_2$  low coordination structure, which enabled exceptional photocatalytic  $\text{CO}_2$ -to- $\text{CH}_4$  conversion.<sup>52</sup> The introduction of Au single atoms enhanced the efficiency of carrier

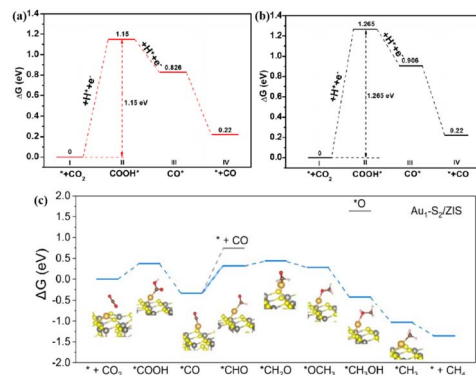


Fig. 3 Free energy diagrams for the reduction of  $\text{CO}_2$  to CO over the (001) facets of  $\text{V}_\text{In}$ -rich-ZIS (a) and  $\text{V}_\text{In}$ -poor-ZIS (b). These figures have been reproduced from ref. 51 with permission from American Chemical Society, copyright 2022. Free energy diagrams of photocatalytic  $\text{CO}_2$  to  $\text{CH}_4$  for  $\text{Au}_1\text{-S}_2/\text{ZIS}$  (c). This figure has been reproduced from ref. 52 with permission from Wiley-VCH, copyright 2022.

separation and transfer. Moreover, the low-coordinated single Au atom significantly enhanced  $\text{CO}_2$  activation, lowered the energy barrier for  $^*\text{CO}$  protonation, and stabilized the  $^*\text{CH}_3$  intermediate, leading to the selective generation of  $\text{CH}_4$  by  $\text{CO}_2$  photoreduction.

Transition metal phosphorous trichalcogenides have been well-explored in the photoreduction of  $\text{CO}_2$  to valuable fuels. The introduction of  $\text{V}_\text{S}$  in  $\text{AgInP}_2\text{S}_6$  regulated the  $\text{CO}_2$  photoreduction reaction pathway to steer the dominant generation of  $\text{C}_2\text{H}_4$ .<sup>54</sup> The  $\text{V}_\text{S}$  led the charge accumulation on the Ag atoms near  $\text{V}_\text{S}$ , which effectively captured the forming  $^*\text{CO}$ . This phenomenon enriched the catalyst surface with key reaction intermediates and promoted C–C coupling to generate  $\text{C}_2$  species with low binding energy barriers. In addition, the tandem synergistic effect of the charge-enriched Cu–In dual site, which was confined on the lateral edge of the  $\text{CuInP}_2\text{S}_6$  monolayer, became the main reason for the efficient conversion and high selectivity of  $\text{C}_2\text{H}_4$ .<sup>55</sup> In the presence of light, the limbic In site of the  $\text{CuInP}_2\text{S}_6$  monolayer converted  $\text{CO}_2$  mainly to  $^*\text{CO}$ , which was transferred to the neighbouring Cu site for the subsequent C–C coupling reaction to  $\text{C}_2\text{H}_4$ .

By reason of the foregoing, MAS in metal chalcogenides shows unique advantages in the generation of  $\text{C}_{2+}$  products. However, due to the limitation of the stability of the metal sulfide, the stability of MAS in them may be lacking. Therefore, in photocatalytic applications, attention should be paid to improving the stability of MAS in metal sulfides.

## 2.3 LDHs

LDHs are typically layered materials consisting of laminates and interlaminar anions with a high degree of flexible tunability in terms of morphology and ionic composition.<sup>57</sup> The adjustment of the metal cation or anion in LDH can easily regulate the electronic structure and influence the  $\text{CO}_2$  conversion process. For example, the selectivity of the photocatalytic reaction could be precisely tuned by the composition of metal cations in the  $\text{ZnM-LDH}$  photocatalysts ( $\text{M} = \text{Ti}^{4+}, \text{Fe}^{3+}, \text{Co}^{3+}, \text{Ga}^{3+}, \text{Al}^{3+}$ ).<sup>56</sup>





Specifically, the main reduction product of ZnTi-LDH was CH<sub>4</sub>. ZnFe-LDH and ZnCo-LDH generated H<sub>2</sub> by water splitting, and ZnGa-LDH and ZnAl-LDH produced CO (Fig. 4a and b). Experimental characterization and theoretical calculations revealed that the d-band center of the M<sup>3+</sup> or M<sup>4+</sup> cations affected the adsorption strength of CO<sub>2</sub>: cations with the d-band centers close to the Fermi level adsorbed CO<sub>2</sub> strongly, benefiting CH<sub>4</sub> or CO formation. Conversely, the deviation of the d-band centre from the Fermi level led to poor CO<sub>2</sub> adsorption and hence H<sub>2</sub> production. In addition, the strategies involving morphology modulation, heterostructure construction, doping, and defect introduction have a crucial effect on the CO<sub>2</sub> conversion process of LDH. The S-scheme heterojunction of g-C<sub>3</sub>N<sub>4</sub>/CoCo-LDH preserved the water oxidation ability of CoCo-LDH and redox ability of g-C<sub>3</sub>N<sub>4</sub>.<sup>58</sup> The atomic-level interface chemical bond (Co–N<sub>2</sub> bond) of g-C<sub>3</sub>N<sub>4</sub>/CoCo-LDH realized the high-speed transfer of electrons. The addition of CoCo-LDH benefited the CO<sub>2</sub> adsorption, reduced the energy barrier of the key intermediate \*COOH, and promoted water decomposition.

Obviously, MAS can take advantage of the two-dimensional (2D) structure, as well as the highly flexible adjustability in the morphology and ionic composition of LDH. However, the synergies of different metals and their roles in C<sub>2+</sub> generation remain to be explored.

## 2.4 MOF

One of the crystalline porous materials, MOF, which possesses diversified metal ions/clusters and organic linkers, as well as atomically precise and tailorable structures, provides the natural MAS for catalysis.<sup>60</sup> Zirconium-based MOF (PCN-222) hybridized with cellulose acetate (CA@PCN-222) increased the activity of CO<sub>2</sub> photoreduction to formate compared with pristine PCN-222 by regulating the atomic interface structure of the MAS (Fig. 5a).<sup>59</sup> The valence band (VB) across the Fermi energy levels resulted in higher charge-transfer kinetics of CA@PCN-222 relative to PCN-222. The interfacial electron transfer from

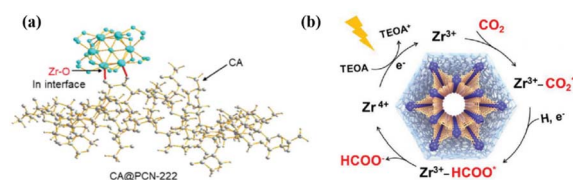


Fig. 5 (a) Schematic atomic interface model of CA@PCN-222. (b) Proposed mechanism for the CO<sub>2</sub> photoreduction reaction over CA@PCN-222. These figures have been reproduced from ref. 59 with permission from Wiley-VCH, copyright 2023.

CA to PCN-222 led to the redistribution of the Zr d-orbital electrons. Moreover, the Zr<sup>IV</sup>-cluster unit in CA@PCN-222 was turned into a Zr<sup>III</sup>-cluster active site after accepting two electrons from two adjacent tetrakis(4-carboxyphenyl)-porphyrin ligands under visible-light irradiation, which selectively reduced CO<sub>2</sub> to HCOO<sup>−</sup> in a two-electron process (Fig. 5b).

The modulation of the coordination environment around the MAS in MOFs helps to reveal the relationship between structure and activity during CO<sub>2</sub> photoreduction. In UiO-type MOFs bearing bipyridine linkers, the number of coordinated N atoms around a single Co site was tuned to provide UiO-Co-N<sub>x</sub> (x = 2, 3 and 4) for photocatalytic CO<sub>2</sub> reduction.<sup>61</sup> UiO-Co-N<sub>3</sub> exhibited superior activity to the other counterparts, which was mainly attributable to the difference in the number of coordinating N atoms around the Co site. Particularly, UiO-Co-N<sub>3</sub> endowed the lowest energy barriers of the rate-determining step (CO<sub>2</sub> → COOH\*) and the desorption of CO\* among all UiO-Co-N<sub>x</sub> samples, accounting for the optimized CO<sub>2</sub> photoreduction activity.

The MAS in MOF enables liquid C<sub>2+</sub> generation. The specific NH<sub>2</sub>–Cu–NH<sub>2</sub> triple atom site was constructed by incorporating Cu sites into the connected nodes of defective UiO-66-NH<sub>2</sub>, realizing photocatalytic CO<sub>2</sub>-to-acetone conversion.<sup>62</sup> Specifically, one of the N active sites on the NH<sub>2</sub>–Cu–NH<sub>2</sub> adsorbed CO<sub>2</sub> and converted CO<sub>2</sub> to form \*CH<sub>3</sub> (CO<sub>2</sub> → COOH\* → CO\* → \*CH<sub>3</sub>). Meanwhile, the Cu site activated its adsorbed CO<sub>2</sub> to CO\*. \*CH<sub>3</sub> and \*CO underwent the first C–C coupling on CuN<sub>2</sub>O<sub>2</sub> to generate \*CO–\*CH<sub>3</sub>. At the same time, another N site on the CuN<sub>2</sub>O<sub>2</sub> fragment activated the adsorbed CO<sub>2</sub> into CO\*, which underwent a second C–C coupling process with the \*COCH<sub>3</sub> intermediate to generate the crucial \*COCOCH<sub>3</sub>. Due to the synergistic interaction between the Cu site and the N site, the C<sub>2</sub> intermediate on the CuN<sub>2</sub>O<sub>2</sub> ultimately generated C<sub>3</sub>.

In summary, the MAS in MOF connected with organic ligands exhibits good dispersion and high utilization, which can make full use of the porous property of MOF to optimize the photocatalytic CO<sub>2</sub> reduction performance. However, its synthesis process involves complex chemical reactions and utilizes expensive organic ligands, making practical production applications difficult.

## 2.5 COF

COF is a class of organic polymers linked by reversible covalent bonds, which possesses periodical structures, well-defined porosity, an extended π-conjugated framework, and pore

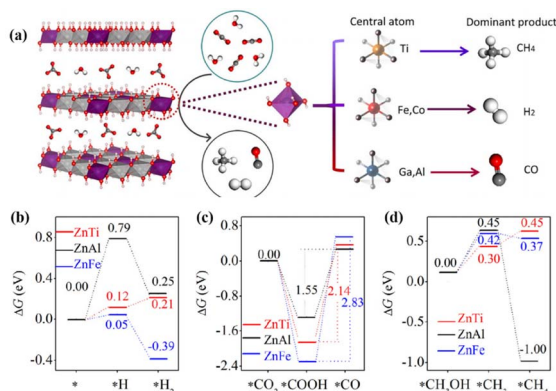


Fig. 4 (a) Scheme showing CO<sub>2</sub> and H<sub>2</sub>O photoreduction on the different ZnM-LDH photocatalyst (carbon: dark gray; oxygen: red; hydrogen: white). DFT calculations of the elementary steps of (b) H<sub>2</sub> evolution, (c) CO<sub>2</sub> reduction to CO, and (d) CO<sub>2</sub> reduction to CH<sub>4</sub> involving a methanol intermediate over ZnTi-LDH, ZnAl-LDH, and ZnFe-LDH. These figures have been reproduced from ref. 56 with permission from Elsevier, copyright 2020.



structures for mass transfer. An adequate MAS of COF could be constructed by incorporating metal atoms into the skeletons or pore channels by coordination interaction.<sup>63</sup> 2D COF ultrathin nanobelts coordinated with single Cu–O/N sites (Cu<sup>2+</sup> anchored by both O and N) exhibited high CO selectivity of 94% under visible-light-driven CO<sub>2</sub> reduction.<sup>64</sup> Crucially, the Cu–O/N sites benefited the electron transfer from COF upon light irradiation, and served as the active sites for the highly selective reduction of CO<sub>2</sub> to CO. Two types of cobalt Schiff base COF composites, Co-2,3-DHTA-COF with Co–O<sub>4</sub> sites and Co-TP-COF with Co–O<sub>3</sub>N sites, realized the CO<sub>2</sub> photoreduction into CO (Fig. 6).<sup>65</sup> The supereminent photocatalytic performance of Co-COF with Co–O<sub>4</sub> sites was mainly attributed to the high CO<sub>2</sub> adsorption capacity, low charge-transfer resistance, strong separation of electrons and holes, and the lower energy barrier in the ligand exchange process between Co-2,3-DHTA-COF and CO<sub>2</sub>. For hydrocarbon product generation, single-atom MoN<sub>2</sub> sites were introduced into COF (Mo-COF) to realize the photoreduction of CO<sub>2</sub> to CH<sub>4</sub> and C<sub>2</sub>H<sub>4</sub> under visible light.<sup>66</sup> The MoN<sub>2</sub> sites contributed to the efficient separation efficiency of photo-generated electrons and holes, enhanced the adsorption and activation of CO<sub>2</sub> and CO, and reduced the energy barriers for the formation of hydrocarbon intermediates, thus leading to the production of high value-added hydrocarbons over Mo-COF.

Particularly, MAS can utilize the  $\pi$ -conjugated framework in COF to promote the photogenerated carrier separation and enhance the photocatalytic CO<sub>2</sub> reduction. However, MAS needs to be grafted onto the COF structure with fine regulation. In addition, the construction of multiple MAS in COF and the study of their catalytic mechanism still need to be continuously explored.

## 2.6 Single-atom catalysts

Single-atom catalysis with MAS uniformly and individually loaded on a supporting material provides a research platform for structure–performance correlation at the atomic level. Atomically dispersed MAS improves the atomic utilization, modulates the charge distribution of the catalyst, and affects the adsorption and conversion of reactants and intermediates, ultimately influencing the product efficiency and selectivity of the photocatalytic CO<sub>2</sub> reduction.

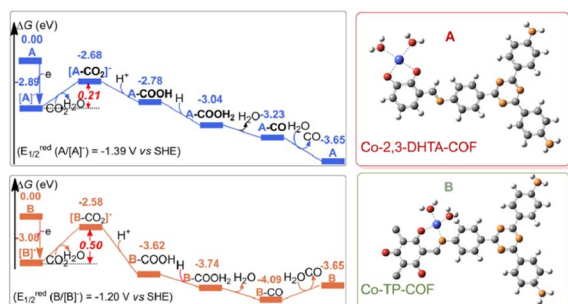


Fig. 6 Gibbs energy profiles of the CO<sub>2</sub>RR-to-CO reaction over Co-2,3-DHTA-COF (A, blue line) and Co-TP-COF (B, orange line). This figure has been reproduced from ref. 65 with permission from American Chemical Society, copyright 2023.

Loading rare-earth La single atoms on carbon nitride (O/La–CN) constructed the active centers of La–N charge-transfer bridges for photocatalytic CO<sub>2</sub> reduction.<sup>67</sup> Electronic state changes induced by the hybridization of the 4f and 5d orbitals of La single atoms and the p–d orbitals of La–N atoms established charge-transfer channels for La–N bridges to promote carrier separation. Bader charge and differential charge distributions suggested that electrons were transferred through La atoms into connected N atoms, and eventually through C atoms to O atoms. The O/La–CN strengthened CO<sub>2</sub> adsorption, endowed the high capacity for CO<sub>2</sub> uptake, and reduced the activation energy barrier for COOH\* formation. Moreover, the desorption of CO from the surface of O/La–CN required the lowest energy (0.2 eV) compared with the dissociation reaction (COH\*, 2.96 eV and C\* + H<sub>2</sub>O, 4.59 eV) or hydrogenation (HCO\*, 1.53 eV), contributing CO formation with high selectivity (Fig. 7a). Cu loading on BiOBr nanosheets (Cu<sub>1</sub>@BiOBr) established a strong built-in electric field with isolated Cu sites that acted as electron traps to promote charge transfer and stabilize charge carriers.<sup>68</sup> The high selectivity of methanol within this photocatalytic system could be ascribed to the energy-favorable hydrogenation of the \*CO intermediate into \*CHO (Fig. 7b). Furthermore, the unfavorable adsorption of CH<sub>3</sub>OH on Cu<sub>1</sub>@BiOBr relative to H<sub>2</sub>O prevented methanol from being oxidized by photogenerated holes.

In addition to single MAS loading, dual MAS incorporation has been explored to drive CO<sub>2</sub> photoreduction with diverse functions. The dual MAS of cobalt (Co) and ruthenium (Ru) supported on a conjugated porous carbon nitride polymer exhibited efficient photocatalytic CO<sub>2</sub> reduction.<sup>69</sup> *In situ* characterizations and theoretical calculations revealed that the active Co sites facilitated dynamic charge transfer, along with Ru working as adsorption sites for CO<sub>2</sub> photoactivation. In detail, the atomic Co facilitated dynamic electron transfer from

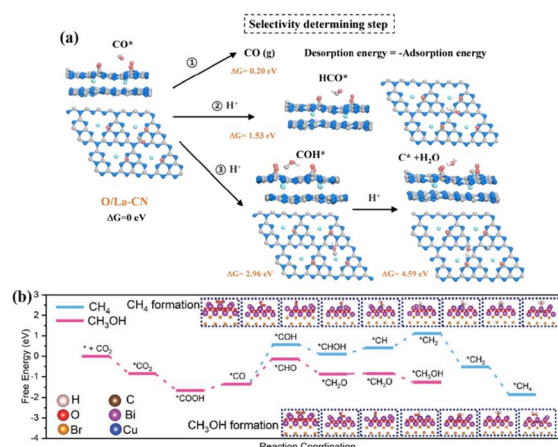


Fig. 7 (a) Calculated free energy for the photocatalytic CO<sub>2</sub> reduction reaction of the selectivity-determining step. This figure has been reproduced from ref. 67 with permission from American Chemical Society, copyright 2020. (b) The DFT-calculated free energy diagram for the hydrogenation of CO<sub>2</sub> to CH<sub>3</sub>OH and CH<sub>4</sub> over Cu<sub>1</sub>@BiOBr. This figure has been reproduced from ref. 68 with permission from Wiley-VCH, copyright 2023.

the carbon nitride polymer to the atomic Ru site, resulting in the COOH\* intermediate being effectively stabilized by the charged-rich Ru site. Moreover, the smaller Gibbs free energy of CO formation than that of the protonation of CO\* to CHO\* resulted in high CO selectivity. Similarly, Ru and Cu single atoms simultaneously incorporated into polymeric carbon nitride (poly-CN) exhibited higher selectivity (95%) for CH<sub>4</sub> production than that decorated with Ru or Cu individually.<sup>70</sup> The atomically dispersed Ru-N<sub>4</sub> and Cu-N<sub>3</sub> sites tuned the electronic structure of poly-CN, and were identified as active centers. During CO<sub>2</sub> photoreduction, the Ru single atom was essential for proton production, while the Cu single atom played a dominant role in the reduction process. Due to the thermodynamically more favorable conversion of \*CO to \*CHO, the coexistence of the Ru and Cu single atoms resulted in the efficient conversion of CO<sub>2</sub> to CH<sub>4</sub>.

Remarkably, the MAS in single-atom catalysts exhibits high metal atom utilization and achieves synergistic effects of multiple MASs. However, the metal is easily aggregated to form particles during the construction process. Thus, a delicate experimental design is required to successfully construct MAS in single-atom form.

## 2.7 Metal complexes

The realization of CO<sub>2</sub> photoreduction by transition metal complexes with tunable and definable chemical structures is accompanied by the activation and immobilisation of neutral CO<sub>2</sub> molecules at the metal centre.<sup>71</sup> By installing a 2-phenol, 2-amino or 2-mercapto to a tripodal skeleton, the Co-based homogeneous catalysts (named [CoN<sub>3</sub>O]ClO<sub>4</sub>, [CoN<sub>4</sub>]ClO<sub>4</sub> and [CoN<sub>3</sub>S]ClO<sub>4</sub>, respectively) possessed different coordination microenvironments for CO<sub>2</sub> reduction.<sup>72</sup> The optimal [CoN<sub>3</sub>O]ClO<sub>4</sub> photocatalyst had a maximum turnover number (TON) of 5652 in photocatalytic CO<sub>2</sub> reduction among [CoN<sub>4</sub>]ClO<sub>4</sub> and [CoN<sub>3</sub>S]ClO<sub>4</sub>. The strong electronegativity of the oxygen atom in the ligand endowed the Co(II) catalytic center with a low reduction potential and more stable \*COOH intermediate, thus substantially promoting the CO<sub>2</sub>-to-CO conversion. The dinuclear heterometallic [CuNiL<sup>2</sup>] showed the highest CO<sub>2</sub>-to-CO conversion relative to dinuclear homometallic [Ni<sub>2</sub>L<sup>2</sup>(CH<sub>3</sub>-OH)<sub>2</sub>] and mononuclear [NiL<sup>1</sup>(CH<sub>3</sub>OH)].<sup>73</sup> A theoretical calculation revealed that the introduction of inactive Cu<sup>II</sup> in CuNi-L<sup>2</sup> promoted the transportation of photo-generated electrons to the coupled active Ni<sup>II</sup> site. This allowed Ni<sup>II</sup> with an O<sub>4</sub> coordination environment in [CuNiL<sup>2</sup>] to express strong reducing ability, which significantly accelerated the photocatalytic CO<sub>2</sub>-to-CO conversion.

Metal complexes could drive C-C coupling to generate C<sub>2+</sub> products. The synergistic dual sites of rhenium(I) bipyridine fac-[ReI(bpy)(CO)<sub>3</sub>Cl] (Re-bpy) and copper porphyrinic triazine framework [PTF(Cu)] working in tandem strategy achieved the photocatalytic conversion of CO<sub>2</sub> to C<sub>2</sub>H<sub>4</sub> (Fig. 8).<sup>74</sup> The CO generated at the Re-bpy sites was adsorbed by the nearby Cu single sites in PTF(Cu), followed by a synergistic C-C coupling process to ultimately produce C<sub>2</sub>H<sub>4</sub>. Critically, Re-bpy-\*CO could enter the porous PTF(Cu) and move to the nearby Cu-\*CO,

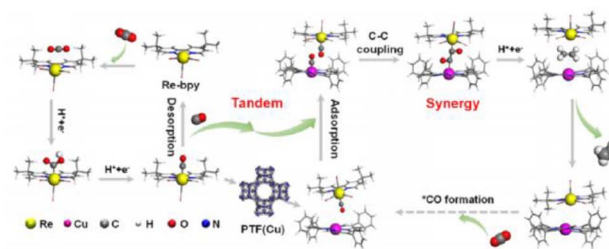


Fig. 8 Tandem catalysis mechanism of Re-bpy/PTF(Cu). This figure has been reproduced from ref. 74 with permission from American Chemical Society, copyright 2023.

leading to practicable free energy for the CO-CO coupling between Cu-\*CO and Re-bpy-\*CO (Re-bpy-\*CO-\*CO-PTF(Cu)). However, PTF(Cu) catalysts alone produced CO under similar conditions. This was caused by the large distance between the adjacent Cu centers in PTF(Cu) hindering C<sub>2+</sub> formation *via* the coupling of Cu-\*CO-\*CO-Cu.

As mentioned above, the alteration of the MAS coordination environment can be achieved by modulating the skeleton in metal complexes, which in turn regulates the photocatalytic CO<sub>2</sub> reduction performance. It is conducive to revealing the in-depth reaction mechanism. However, the typical problems in photocatalysis, such as the high separation cost and low chemical stability, still limit their practical applications.<sup>75</sup>

## 3 Different formulations of MAS in the photocatalytic CO<sub>2</sub> reduction

Incorporation of MAS can regulate the transport of photo-generated carriers, increase the local electron density of the adsorption sites, affect the adsorption strength of reactants and intermediates, and ultimately adjust the barrier and selectivity of the reaction. In this section, the role of different formulations of MAS in photocatalytic CO<sub>2</sub> reduction is described in detail (Table 1).

### 3.1 Single MAS

The incorporation of individual MAS into the catalyst backbone from an atomic level perspective maximizes atomic utilisation efficiency and optimizes the performance of photocatalytic CO<sub>2</sub> conversion. The bipyridine-based polyimide polymer (Bpy-PDI) anchoring single Ni site achieved diluted CO<sub>2</sub> photoreduction with high generation activity for CO<sub>2</sub>-to-CO in 0.1 atm CO<sub>2</sub> pressure.<sup>76</sup> The obviously larger adsorption energy of CO<sub>2</sub> for the Ni site (1.44 eV) compared to that of Bpy-PDI (0.19 eV) indicated a much stronger adsorption affinity of the Ni site towards CO<sub>2</sub>. Moreover, the free energy of COOH\* generation (the rate-determining step) on the Ni sites (-0.07 eV) was obviously smaller than that of Bpy-PDI (1.69 eV), revealing the contribution of the dispersed Ni atom toward the energy barrier decline. Cu single atoms on the nitrogen-doped carbon anchored on TiO<sub>2</sub> with the anatase-rutile mixed phase exhibited 100% CO selectivity in the photocatalytic CO<sub>2</sub> reduction.<sup>77</sup> Cu single atoms became the adsorption and activation sites for





Table 1 Different formulations of MAS in photocatalytic CO<sub>2</sub> reduction

Single MAS	Catalyst	Reactive sites	Light source	Reaction condition	Performance ( $\mu\text{mol g}^{-1} \text{h}^{-1}$ )	Ref.
Cu-doped ZnS containing abundant S-W junctions	Cu	Cu	300 W Xe lamp	18 mL solution containing chloroform + 2 mL 2-propanol + CO <sub>2</sub>	CO: 68.9 (99.9%)	49
V <sub>In</sub> -rich-ZIS	V <sub>In</sub>	V <sub>In</sub>	300 W Xe lamp AM 1.5 cut-off filter	45 mL acetonitrile (MeCN) + 5 mL triethylamine (TEOA) + CO <sub>2</sub>	CO: 298	51
ZnM-LDH (M = Ti <sup>4+</sup> , Ga <sup>3+</sup> , Al <sup>3+</sup> )	M	M	300 W Xe lamp	0.1 mL H <sub>2</sub> O + 0.08 MPa CO <sub>2</sub>	CH <sub>4</sub> : 1.2 (68% M = Ti) (90% M = Al), CO: 1.6 (78% M = Ga)	56
CA@PCN-222	Zr <sup>III</sup> -cluster	Zr <sup>III</sup> -cluster	300 W Xe lamp (800 nm > $\lambda$ > 400 nm)	60 mL mixed solution (MeCN/TEOA = 30/1) + CO <sub>2</sub>	HCOO <sup>-</sup> : 281.6	59
UiO-Co-N <sub>3</sub>	Co-N <sub>3</sub>	Co-N <sub>3</sub>	300 W Xe lamp ( $\lambda \geq 420$ nm)	20 mL MeCN + 30 mg [Ru(bpy) <sub>3</sub> ]Cl <sub>2</sub> · 6H <sub>2</sub> O + 0.025 M 1,3-dimethyl-1,3-dihydro-2-phenyl-2H-benzimidazole (BIH) + CO <sub>2</sub>	CO: 179.3 (99.3%)	61
Incorporating Cu sites into the connected nodes of defective UiO-66-NH <sub>2</sub>	NH <sub>2</sub> -Cu-NH <sub>2</sub>	NH <sub>2</sub> -Cu-NH <sub>2</sub>	300 W Xe lamp ( $\lambda > 420$ nm)	2 mL H <sub>2</sub> O + 6 mL N,N'-dimethylformamide (DMF) + CO <sub>2</sub>	CH <sub>3</sub> COCH <sub>3</sub> : 70.9 (97%)	62
2,2'-Bipyridine-based COF bearing non-noble single Cu sites	Cu <sup>2+</sup> sites	Cu <sup>2+</sup> sites	300 W Xe lamp ( $\lambda > 420$ nm)	10 mL DMF or H <sub>2</sub> O + 1 mL triethylamine + CO <sub>2</sub>	CH <sub>4</sub> : 17.5; CO: 1.6 (H <sub>2</sub> O), CO: 10.2 (100%; DMF), CO: 22.5 (66.4%); DMF/H <sub>2</sub> O = 50%	63
Cu-COF	Cu-O/N sites	Cu-O/N sites	300 W Xe lamp ( $\lambda > 420$ nm)	12 mL mixed solution + 600 torr CO <sub>2</sub> , MeCN/H <sub>2</sub> O/TEOA (8 mL/2 mL/2 mL)	CO: 206 (94%)	64
Co-2,3-DHTA-COF	Co-O <sub>4</sub> sites	Co-O <sub>4</sub> sites	300 W Xe lamp ( $\lambda > 420$ nm)	46 mL mixed solution + 10 mg [Ru(bpy) <sub>3</sub> ]Cl <sub>2</sub> · 6H <sub>2</sub> O + 1 atm CO <sub>2</sub> , MeCN/H <sub>2</sub> O/TEOA (32 mL/8 mL/6 mL)	CO: 18 000 (95.7%)	65
Mo-COF	MoN <sub>2</sub> sites	MoN <sub>2</sub> sites	300 W Xe lamp ( $\lambda \geq 420$ nm)	5 mL H <sub>2</sub> O + 1 mL CO <sub>2</sub>	CO: 6.19, C <sub>2</sub> H <sub>4</sub> : 3.57, CH <sub>4</sub> : 1.08	66
O/La-CN	La-N charge-transfer bridge	La-N charge-transfer bridge	Xe lamp	12 mL mixed solution + 1 atm CO <sub>2</sub> , MeCN/H <sub>2</sub> O/TEOA (6 mL/4 mL/2 mL)	CO: 92 (80.3%)	67
Cu <sub>1</sub> @BiOBr [Co <sub>3</sub> O]ClO <sub>4</sub>	Isolated Cu sites Co(II) catalytic center	Isolated Cu sites Co(II) catalytic center	300 W Xe lamp 300 W Xe lamp ( $\lambda > 420$ nm)	5 mL H <sub>2</sub> O + 4 MPa CO <sub>2</sub> 5 mL mixed solution + [Ru(bpy) <sub>3</sub> ]Cl <sub>2</sub> · 6H <sub>2</sub> O + BIH + CO <sub>2</sub> MeCN/H <sub>2</sub> O (4 mL/1 mL)	CH <sub>3</sub> OH: 627.66 (86.6%) CO: 88.14% $\pm$ 2.09%	68 72
CuNi-L <sup>2</sup>	Active Ni <sup>II</sup> site	Active Ni <sup>II</sup> site	LED light ( $\lambda > 420$ nm)	25 mL mixed solution + [Ru(bpy) <sub>3</sub> ]Cl <sub>2</sub> · 6H <sub>2</sub> O (0.85 mmol L <sup>-1</sup> ) + Triisopropanolamine (TIPA)	CO: (93.5%)	73
Cu single atoms on the nitrogen-doped carbon anchored on TiO <sub>2</sub>	Cu SAS	Cu SAS	300 W Xe lamp	0.8 mol L <sup>-1</sup> + CO <sub>2</sub> , MeCN/H <sub>2</sub> O (20 mL/5 mL) H <sub>2</sub> O vapor + CO <sub>2</sub>	CO: 65.8	77
2Re-In <sub>2</sub> O <sub>3</sub>	O <sub>def</sub>	O <sub>def</sub>	300 W Xe lamp	100 mL H <sub>2</sub> O + 1.01 bar CO <sub>2</sub>	CH <sub>3</sub> OH: 265.6 (100%)	78
Cu <sub>1</sub> /TiO <sub>2</sub>	Cu <sub>1</sub> -O <sub>2+1</sub>	Cu <sub>1</sub> -O <sub>2+1</sub>	Xe lamp	20 mL H <sub>2</sub> O + TEOA + CO <sub>2</sub>	C <sub>2</sub> H <sub>4</sub> : 60.4 (75.2%)	79
MIL-88B-NS40	Fe-N coordinated sites/uncoordinated S	Fe-N coordinated sites/uncoordinated S	300 W Xe lamp ( $\lambda > 420$ nm)	2 mL H <sub>2</sub> O + CO <sub>2</sub>	C <sub>2</sub> H <sub>4</sub> : 17.7	80
B-Ni <sub>1</sub> /WO <sub>2.72</sub>	Ni site	Ni site	300 W Xe lamp ( $\lambda > 420$ nm)	6 mL mixed solution + 15 mg [Ru(bpy) <sub>3</sub> ]Cl <sub>2</sub> · 6H <sub>2</sub> O + CO <sub>2</sub> , MeCN/H <sub>2</sub> O/TEOA (3 mL/2 mL/1 mL)	CO: 80 500 (98.7%)	82
Isolated Mn atoms over the multi-edged TiO <sub>2</sub> nano-pompons	Mn atoms	Mn atoms	300 W Xe lamp ( $\lambda > 420$ nm)	6 mL mixed solution + 10 mg [Ru(bpy) <sub>3</sub> ]Cl <sub>2</sub> · 6H <sub>2</sub> O + 1 atm CO <sub>2</sub> , MeCN/H <sub>2</sub> O/TEOA (3 mL/2 mL/1 mL)	CO: 80 510, H <sub>2</sub> : 23 070	83
In-bonded N-atom (In <sup>δ+</sup> -N <sub>i</sub> ) in the (002) crystal planes of g-C <sub>3</sub> N <sub>4</sub>	In <sup>δ+</sup> -N <sub>i</sub>	In <sup>δ+</sup> -N <sub>i</sub>	300 W Xe lamp	400 $\mu$ L H <sub>2</sub> O + CO <sub>2</sub>	CO: 398.87	84





Table 1 (Contd.)

Catalyst	Reactive sites	Light source	Reaction condition	Performance ( $\mu\text{mol g}^{-1} \text{h}^{-1}$ )	Ref.
CuACs/PCN 3Er-ZnIn <sub>2</sub> S <sub>4</sub>	Cu-N <sub>3</sub> sites doped P Er	300 W Xe lamp	5 mL TEOA + [Ru(bpy) <sub>3</sub> ]Cl <sub>2</sub> ·6H <sub>2</sub> O + 45 mL H <sub>2</sub> O + CO <sub>2</sub>	C <sub>2</sub> H <sub>4</sub> : 10.17 (53.2%), CH <sub>4</sub> : 9.55	85
		300 W Xe lamp ( $\lambda \geq 420$ nm)	TEOA + 100 mL H <sub>2</sub> O + 80 kPa CO <sub>2</sub>	CH <sub>4</sub> : 6.68 (>90%)	86
Cu <sub>1</sub> N <sub>3</sub> @PCN Ag <sub>1</sub> @PCNT	Different coordination structures Cu-atom Ag-N <sub>3</sub> , Ag single atoms	300 W Xe lamp ( $\lambda > 420$ nm)	1 mL H <sub>2</sub> O + CO <sub>2</sub>	CO: 49.8	87
		300 W Xe lamp AM 1.5 cut-off filter	3 mL H <sub>2</sub> O + 70 kPa CO <sub>2</sub>	CO: 160 (>94%)	88
Ultra-high Pr loading CN MCOF-Ti <sub>6</sub> Cu <sub>3</sub>	Pr <sub>1</sub> -N <sub>4</sub> O <sub>2</sub> sites Cu cluster	300 W Xe lamp	1.0 mL H <sub>2</sub> O + 4.0 mL CO <sub>2</sub>	CH <sub>3</sub> OH: 511.1	89
		Xe lamp AM 1.5 cut-off filter	30 mL H <sub>2</sub> O + CO <sub>2</sub>	HCOOH: 169.8	90
Dual MAS Mn <sub>1</sub> Co <sub>1</sub> /CN	Two compatible active centers of Mn and Co	300 W Xe lamp ( $\lambda > 400$ nm)	2 mL H <sub>2</sub> O + 80 kPa CO <sub>2</sub>	CO: 47	17
		300 W Xe lamp	12.5 mL MeCN + 2.5 mL H <sub>2</sub> O + 1 atm CO <sub>2</sub>	C <sub>2</sub> H <sub>4</sub> : 7.6, C <sub>3</sub> H <sub>8</sub> : 13.8, CO: 18.6	46
Cu-Ti-V <sub>2</sub> O <sub>7</sub> /Ti <sub>0.91</sub> O <sub>2</sub> -SL CuInP <sub>2</sub> S <sub>6</sub> monolayer	Cu-Ti-V <sub>2</sub> O <sub>7</sub> unit Cu-In dual site	300 W Xe lamp	0.4 mL H <sub>2</sub> O + CO <sub>2</sub>	C <sub>2</sub> H <sub>4</sub> : 20.89 (56.4%), CO: 8.59,	55
		AM 1.5 cut-off filter		CH <sub>4</sub> : 6.22	
V into NiAl-LDH	V; lower-valence Ni	300 W Xe lamp ( $\lambda > 400$ nm)	10 mL mixed solution + 0.005 mmol [Ru(bpy) <sub>3</sub> ] Cl <sub>2</sub> ·6H <sub>2</sub> O + 1.8 bar CO <sub>2</sub> MeCN/H <sub>2</sub> O/TEOA (6 mL/2 mL/ 2 mL)	CH <sub>4</sub> : 217 (78.9%)	57
Dispersed Co-Ru bimetal into conjugated porous carbon nitride polymer	Co sites; Ru sites	300 W Xe lamp	500 $\mu\text{L}$ H <sub>2</sub> O + 70–80 kPa CO <sub>2</sub>	CO: 27.3	69
Ru Cu single atom incorporated into polymeric carbon nitride	Ru-N <sub>4</sub> sites, Cu-N <sub>3</sub> sites	300 W Xe lamp	9 mL NaHCO <sub>3</sub> (3 M) + 1 mL TEOA + CO <sub>2</sub>	CH <sub>4</sub> : 154 (95%), CO: 2, H <sub>2</sub> : 6	70
Re-bpy/PTF(Cu)	Re-bpy sites; Cu single sites in PTF(Cu)	300 W Xe lamp (1100 nm > $\lambda$ > 2.5 mL) 400 nm)	5 mL mixed solution + 1 atm CO <sub>2</sub> MeCN/TEOA (2.5 mL/ 2.5 mL)	C <sub>2</sub> H <sub>4</sub> : 73.2	74
Cu-N <sub>2</sub> -V LaNi-Phen/COF-5	Cu <sup>+</sup> /Cu <sup>2+</sup> Optically active (La site) catalytically active (Ni site)	300 W Xe lamp	21 mL DMF + 3 mL H <sub>2</sub> O + 0.8 MPa CO <sub>2</sub>	C <sub>2</sub> H <sub>5</sub> OH: 69.8	81
		300 W Xe lamp	10 mM BIH + 48 mL MeCN + 2 mL H <sub>2</sub> O + 80 kPa CO <sub>2</sub>	CO: 605.8 (98.2%)	91
CuIn <sub>5</sub> S <sub>8</sub> Ag <sub>2</sub> Cu <sub>2</sub> O <sub>3</sub>	Cu-In dual sites Cu-Ag Lewis acid-base dual sites	300 W Xe lamp ( $\lambda > 400$ nm)	2 mL H <sub>2</sub> O + 0.1 atm CO <sub>2</sub>	CH <sub>4</sub> : 8.7	92
		300 W Xe lamp	5 mL H <sub>2</sub> O or 5 mL 0.2% methanol aqueous solution was injected + CO <sub>2</sub>	CH <sub>4</sub> : 3.6	93
In/TiO <sub>2</sub> -Vo	Vo-regulated In-Ti dual sites	Xe lamp (320 nm < $\lambda$ < 780 nm)	H <sub>2</sub> O + CO <sub>2</sub>	CH <sub>4</sub> : 35.49 (91.3%)	94
Au/Co dual single atom loaded Cds NPs	Au/Co DSA	300 W Xe lamp ( $\lambda > 400$ nm)	CO <sub>2</sub>	CO: 64.1 $\mu\text{mol g}^{-1}$ , CH <sub>4</sub> : 7.7 $\mu\text{mol g}^{-1}$	95
Vo-rich Zn <sub>2</sub> GeO <sub>4</sub> nanobelts	Asymmetric Zn-O-Ge sites	Xe lamp light	12 mL H <sub>2</sub> O + 0.03 vol% CO <sub>2</sub> /Ar gas mixture	CH <sub>3</sub> COOH: 12.7 (29.95%)	96
Au-CeO <sub>2</sub> InCu/PCN	Au-O-Ce sites In-Cu dual sites	300 W Xe lamp	5 mL H <sub>2</sub> O + 80 kPa CO <sub>2</sub>	CO: 11.07, C <sub>2</sub> H <sub>6</sub> : 11.07 (65.3%)	97
		300 W Xe lamp	24 mL DMF/H <sub>2</sub> O (12.5 vol% H <sub>2</sub> O) + 0.8 MPa CO <sub>2</sub> 1.0 mL H <sub>2</sub> O + (CO <sub>2</sub> -1%, N <sub>2</sub> -99%)	C <sub>2</sub> H <sub>5</sub> OH: 28.5 (92%)	98
					99



Table 1 (Contd.)

Catalyst	Reactive sites	Light source	Reaction condition	Performance ( $\mu\text{mol g}^{-1} \text{h}^{-1}$ )	Ref.
$\text{Bi}_2\text{WO}_6$ nanosheets with Vo anchoring Au and Cu dual single atoms	Au–Cu dual-single-atom sites; Vo	300 W Xe lamp (780 nm > $\lambda$ > 320 nm)	15 mL $\text{H}_2\text{O}$ + 0.5 MPa $\text{CO}_2$	Total amount of production ( $\text{CO}$ , $\text{CH}_4$ , $\text{C}_2\text{H}_4$ , $\text{C}_3\text{H}_6$ ): 83.9	100
2% Pd–Cu/ $\text{TiO}_2$	Pd–Cu; Vo	300 W Xe lamp	50 mL $\text{H}_2\text{O}$ (0.1 M $\text{Na}_2\text{SO}_3$ + 0.2 M $\text{C}_6\text{OH}$ ) + $\text{CO}_2$	$\text{CH}_3\text{OH}$ : 71.84 (91.71)	101
Single atoms of Ni/Co loaded on $\text{TiO}_2$	Ni Co single atoms	300 W Xe lamp	1 mL $\text{H}_2\text{O}$ + $\text{CO}_2$	$\text{CH}_3\text{COOH}$ : 22.6, 71%	102
Incorporated the redox-active $\text{Co}^{2+}/\text{Ni}^{2+}$ centers into the chemically stable layered lead iodide hybrids	$\text{Co}^{2+}/\text{Ni}^{2+}$ –O–Pb bimetallic catalytic sites	AM 1.5 G filter		$\text{C}_2\text{H}_5\text{OH}$ : 24.9–31.4, 89.5–93.6%	103
$\text{g-C}_3\text{N}_4/\text{UiO-66}(\text{Zr}/\text{Ce})$	N–Zr/Ce–O	300 W Xe lamp	15 mL $\text{MeCN}$ + 15 mL $\text{H}_2\text{O}$ + 101 kPa $\text{CO}_2$	$\text{CH}_3\text{OH}$ : 54.71, $\text{C}_2\text{H}_5\text{OH}$ : 38.10	104
Cu–CuTCPP/ $\text{g-C}_3\text{N}_4$	$\text{Cu}^{1+6}$	300 W Xe lamp (800 nm > $\lambda$ > 360 nm)	400 $\mu\text{L}$ $\text{H}_2\text{O}$ + 200 $\mu\text{L}$ TEA + 0.1 MPa $\text{CO}_2$	CO: 12.3, $\text{CH}_4$ : 11.6, $\text{C}_2\text{H}_6$ : 18.5	31
MAS combined P and Cu dual sites anchored on graphitic carbon nitride	P–N and Cu–N <sub>4</sub> dual sites	300 W Xe lamp	3 mL TEOA + $\text{H}_2\text{O}$ + 0.65 atm $\text{CO}_2$	$\text{C}_2\text{H}_6$ : 616.6	45
1% Ru– $\text{TiO}_{2-x}$	Ru; Vo	300 W Xe lamp	0.14 g $\text{NaHCO}_3$ + $\text{N}_2$ + $\text{H}_2\text{O}$ + $\text{H}_2\text{SO}_4$ (2 M)	$\text{CH}_4$ : 31.63 (90.93%)	47
A series of metastable $\text{WO}_3$ photocatalysts with the coexistence of S doping and Vo	W–S–W bridge; Vo	300 W Xe lamp	0.4 mL $\text{H}_2\text{O}$ + $\text{CO}_2$	$\text{C}_2\text{H}_4$ : 224.278, 87.6%	52
Au atoms to ultrathin $\text{ZnIn}_2\text{S}_4$ nanosheets with Vs	$\text{Au}_1\text{-S}_2$	300 W Xe lamp ( $\lambda$ > 420 nm)	5 mL mixed solution + 10 mg $[\text{Ru}(\text{bpy})_3\text{Cl}_2 \cdot 6\text{H}_2\text{O} + 1 \text{ CH}_4$ : 275 (77%) atm $\text{CO}_2$ , $\text{MeCN}/\text{H}_2\text{O}/\text{TEOA}$ (3 mL/1 mL/1 mL)	$\text{CH}_4$ : 44.3 (73%)	105
Vs–AgInP <sub>2</sub> S <sub>6</sub> single atomic layer	Ag atoms; Vs	300 W Xe lamp	0.4 mL $\text{H}_2\text{O}$ + $\text{CO}_2$	CO: 40.02 (82.9%)	106
Mn dopants and Vo were engineered in $\text{Zn}_2\text{GeO}_4$ nanorods	Mn dopants and Vo	300 W Xe lamp	1 mL $\text{H}_2\text{O}$ + $\text{CO}_2$	CO: 11.12	107
$\text{Cu}_1/\text{N}_{20}\text{V-CN}$	Cu single atoms; N <sub>20C</sub> vacancies	300 W Xe lamp AM 1.5 cut-off filter	200 $\mu\text{L}$ $\text{H}_2\text{O}$ + 105 kPa $\text{CO}_2$	$\text{C}_2\text{H}_4$ : 335.67 (93.87%)	108
$\text{CuGaS}_2/\text{Ga}_2\text{S}_3$ containing Vs	Cu–Ga metallic bond	300 W Xe lamp ( $\lambda$ > 420 nm)	3 mL $\text{H}_2\text{O}$ + TEOA + 70 kPa $\text{CO}_2$	$\text{CH}_4$ : 12.42	109
$\text{Cu}_{1.95}\text{S}_{1-x}$	Dual Cu and Vs	300 W Xe lamp AM 1.5 cut-off filter	1 atm $\text{CO}_2$		110
MAS synergizing with nanoparticles	Cu nanoparticles; Ni single-atom sites; asymmetric Ni–N <sub>4</sub> sites	300 W Xe lamp ( $\lambda$ > 420 nm)	95 mL $\text{H}_2\text{O}$ + 5 mL TEOA + 100 kPa $\text{CO}_2$	$\text{CH}_4$ : 35.245, CO: 32.067, $\text{C}_3\text{H}_6$ : 25.328	111
$\text{Co}_1\text{Ag}_{(1-n)}\text{PCN}$	Co–N <sub>6</sub> –P bonds, Ag–N <sub>2</sub> C <sub>2</sub> SA sites, Ag NPs	300 W Xe lamp	6 mL $\text{CH}_3\text{CN}$ + 4 mL $\text{H}_2\text{O}$ + 80 kPa $\text{CO}_2$	CO: 46.82 (70.1%)	112
Cu single atoms and nanoclusters supported on defective $\text{TiO}_2$	Cu SAS, Cu NCs	300 W Xe lamp	100 $\mu\text{L}$ $\text{H}_2\text{O}$ + $\text{CO}_2$	$\text{CH}_4$ : 19.63 (98%)	113
single Pd atoms and Pd nanoparticles on graphitic carbon nitride	Pd <sub>1</sub> sites; Pd <sub>NPS</sub> sites	Xe lamp	10 mL $\text{H}_2\text{O}$ + 1 atm $\text{CO}_2$	$\text{CH}_4$ : 20.3 (97.8%)	58
$\text{g-C}_3\text{N}_4/\text{CoCo-LDH}$	Co–N <sub>2</sub> bonds	300 W Xe lamp	3 mL $\text{H}_2\text{O}$ + 1 atm $\text{CO}_2$	CO: 71.39	114
heterostructure $\text{CuO}/\text{Cu}_2\text{V}_2\text{O}_7$	Two metal atomic sites of Cu and V	300 W Xe lamp	20 mL TEOA + 80 mL $\text{H}_2\text{O}$ + 1.01 bar $\text{CO}_2$	CO: 118, $\text{C}_2\text{H}_4$ : 29.57	115
2D/2D Ni-doped $\text{CsPbBr}_3/\text{Bi}_3\text{O}_4\text{Br}$ scheme heterojunction	Ni <sup>2+</sup>	300 W Xe lamp	2 mL $\text{H}_2\text{O}$ + 101 kPa $\text{CO}_2$	CO: 96.89 (98.2%)	115
Co–TCPP/ $\text{Bi}_3\text{O}_4\text{Br}$	Bi–O bridge bond; Co atoms	300 W Xe lamp	50 mL $\text{H}_2\text{O}$ + 0.08 MPa $\text{CO}_2$	CO: 71.3	





Table 1 (Contd.)

Catalyst	Reactive sites	Light source	Reaction condition	Performance ( $\mu\text{mol g}^{-1} \text{h}^{-1}$ )	Ref.
Cu-SAEB	N-Cu <sub>1</sub> -S single-atom electron bridge	300 W Xe lamp	0.1 mL H <sub>2</sub> O + CO <sub>2</sub>	CO: 236.0, O <sub>2</sub> : 120.1	116
In <sub>2</sub> O <sub>3</sub> /CdSe-diethylenetriamine 2D/0D g-C <sub>3</sub> N <sub>4</sub> /Cu <sub>2</sub> SnS <sub>3</sub>	In-O-Cd bonds; Vo	300 W Xe lamp	120 mg NaHCO <sub>3</sub> + 0.5 mL H <sub>2</sub> SO <sub>4</sub>	CO: 70.08, CH <sub>4</sub> : 27.92	117
	Cu-C and Cu-N dual chemical bond; Cu sites	100 W Xe lamp	H <sub>2</sub> O + CO <sub>2</sub>	CO: 18.2	118
NiAl-Fe-TCPP	Fe; Ni	AM 1.5 filter			
		300 W Xe lamp	0.005 mmol [Ru(bpy) <sub>3</sub> ]Cl <sub>2</sub> · 6H <sub>2</sub> O + 10 mL mixed solution + 1.8 bar CO <sub>2</sub> /MeCN/H <sub>2</sub> O/TEOA (6 mL/2 mL/2 mL)	C <sub>2</sub> H <sub>4</sub> : 2470	119
r-In <sub>2</sub> O <sub>3</sub> /InP	O-In-P polarized sites	300 W Xe lamp ( $\lambda > 420$ nm)	100 mL H <sub>2</sub> O + 80 kPa CO <sub>2</sub>	CH <sub>3</sub> COOH: 9.67 (96.1%)	120
CdS:Dy <sup>3+</sup> /g-C <sub>3</sub> N <sub>4</sub>	Dy <sup>3+</sup> single atom	300 W Xe lamp ( $\lambda > 400$ nm)	4 mL H <sub>2</sub> O + CO <sub>2</sub>	CH <sub>4</sub> : 8.06	121
Bi NCS/Bi <sub>2</sub> O <sub>3</sub>	Bi <sup>0</sup> of Bi NCS	300 W Xe lamp ( $\lambda > 420$ nm)	1 mL H <sub>2</sub> O + 0.08 MPa CO <sub>2</sub>	CH <sub>4</sub> : 7.45 (94.8%)	122
CsCuCl <sub>3</sub> /Cu NCS	Cu NCS	150 W Xe lamp	4 mL ethyl acetate (EA) + 1 mL propan-2-ol (IPA) + CO <sub>2</sub>	CH <sub>4</sub> : 7.2 (92.7%)	123
		AM 1.5 cut-off filter			
Ultrathin Bi <sub>12</sub> O <sub>17</sub> Cl <sub>2</sub> nanosheets	Vo; Bi clusters	300 W Xe lamp	50 mL H <sub>2</sub> O + 0.08 MPa CO <sub>2</sub>	CO: 64.3	124
Bi-BiOCl plasmonic nanoparticles decorated TiO <sub>2</sub> nanosheets	Bi	300 W Xe lamp	5 mL 0.2 M NaHCO <sub>3</sub> + CO <sub>2</sub>	CH <sub>3</sub> OH: 235.78 ( $\approx 90\%$ )	125
		AM 1.5 cut-off filter			
Au/TiO <sub>2</sub> /W <sub>18</sub> O <sub>49</sub>	Au-O-Ti, W-O-Ti	300 W Xe lamp ( $\lambda > 420$ nm)	0.1 mL H <sub>2</sub> O + CO <sub>2</sub>	CH <sub>4</sub> : 35.55, CO: 2.57, CH <sub>4</sub> (93.3%)	126
PtAg <sub>2</sub> /HNb <sub>3</sub> O <sub>8</sub>	Pt-Ag alloy (7 : 43 Pt-Ag molar ratio)	300 W Xe lamp (320 nm < $\lambda$ < 780 nm)	2 mL H <sub>2</sub> O + 0.09 MPa CO <sub>2</sub>	CH <sub>4</sub> : 93.6 (74.3%)	127
PtCu/TiO <sub>2</sub>	Pt/Cu alloy (0.4 : 0.6)	300 W Xe lamp (300 nm < $\lambda$ < 400 nm)	Water vapor + CO <sub>2</sub>	CH <sub>4</sub> : 100%	128
Cu-Ag/TiO <sub>2</sub>	Cu-Ag alloy (0.8 : 0.2)	300 W Xe lamp (AM 1.5 cut-off filter)	150 mL H <sub>2</sub> O + 90 kPa CO <sub>2</sub>	C <sub>2</sub> H <sub>4</sub> : 1110.6	129
AuIr with InGaN nanowires on silicon	Au <sub>3</sub> Ir <sub>1</sub> alloy (0.44 : 0.56)	300 W Xe lamp	30 mL H <sub>2</sub> O + 2 atm CO <sub>2</sub>	C <sub>2</sub> H <sub>6</sub> : 58 800, CH <sub>4</sub> : 125 400, H <sub>2</sub> : 735 600, CO: 127 800	130
Au/TZO	Au nanoparticles	300 W Xe lamp	20 mL mixed solution + 1 atm CO <sub>2</sub>	H <sub>2</sub> : 271.6, CO: 260.6, C <sub>2</sub> H <sub>4</sub> : 6.80, C <sub>2</sub> H <sub>6</sub> : 4.05	131
		AM 1.5 G filter	(16 mL/2 mL/2 mL)		
Bi nanoparticles grown on the Bi <sub>2</sub> MoO <sub>6</sub> with Vo	Bi nanoparticles Vo	Xe lamp	0.42 g NaHCO <sub>3</sub> + 30 mL H <sub>2</sub> O + CO <sub>2</sub>	C <sub>2</sub> H <sub>5</sub> OH: 17.93 (92%)	132

CO<sub>2</sub>, where the strong hybridization of the Cu 3d and CO<sub>2</sub>-O 2p orbitals facilitated the transfer of electrons from the Cu single atoms to CO<sub>2</sub>, effectively optimizing the rate-limiting step (CO<sub>2</sub>\* → COOH\*). Moreover, single MAS also improved the selectivity of the liquid product of the photocatalytic CO<sub>2</sub> reduction. The atomically dispersed rhenium (Re) in In<sub>2</sub>O<sub>3</sub> changed the product from CO on pure In<sub>2</sub>O<sub>3</sub> to CH<sub>3</sub>OH on 2Re-In<sub>2</sub>O<sub>3</sub>.<sup>78</sup> DFT calculations disclosed that the Re site promoted the H<sub>2</sub>O dissociation to form sufficient H atoms for CO<sub>2</sub> reduction. Critically, CO preferred to be hydrogenated into CHO instead of desorption due to the strong binding between CO and Re<sub>1</sub>-In<sub>2</sub>O<sub>3</sub>(111). Through multi-step hydrogenation, CHO was eventually converted to CH<sub>3</sub>OH with high selectivity.

Photocatalytic CO<sub>2</sub> conversion mainly involves C=O bond cleavage and C-H bond formation, accompanied by the challenging C-C coupling toward the generation of C<sub>2+</sub> products. The MAS could reduce electrostatic repulsion between the C<sub>1</sub> intermediates, promote C-C coupling, and thus lead to the highly selective formation of the C<sub>2+</sub> product. The photo-generated electron transition from TiO<sub>2</sub> to atomically dispersed Cu atoms rearranged the energy levels of the Cu 3d orbitals.<sup>79</sup> Consequently, the initial four-coordinated Cu<sub>1</sub>-O<sub>4</sub> was distorted into a Cu<sub>1</sub>-O<sub>2+1</sub> structure (twofold normal Cu-O coordination and one stretched Cu-O coordination), which could be reversibly recovered after removing the synergistic light field. The photoinduced metastable intermediate of Cu<sub>1</sub>-O<sub>2+1</sub> delivered an C<sub>2</sub>H<sub>4</sub> yield rate of 60.4 μmol gcat<sup>-1</sup> h<sup>-1</sup>. The energy barrier of the first protonation step from CO<sub>2</sub> to \*COOH showed an obvious decline over Cu<sub>1</sub>-O<sub>2+1</sub>, indicating the stronger activation capability of the metastable asymmetrical structure to reactants than that of Cu<sub>1</sub>-O<sub>4</sub>. \*CO molecules adsorbed more strongly on the Cu<sub>1</sub>-O<sub>2+1</sub> (-1.49 eV) surface than on the Cu<sub>1</sub>-O<sub>4</sub> (-0.44 eV) surface, leading to subsequent hydrogenation rather than desorption. It was noteworthy that, in contrast to Cu<sub>1</sub>-O<sub>4</sub>, Cu<sub>1</sub>-O<sub>2+1</sub> promoted C-C coupling and further formation of C-C bonds, thus facilitating the generation of C<sub>2</sub>H<sub>4</sub>. Furthermore, N,S-codoped Fe-MOF MIL-88B with a well-defined bipyramidal hexagonal prism shape was designed.<sup>80</sup> The synergistic effect of the Fe-N coordinated sites and reasonable defects from uncoordinated S increased the electron density disorder around Fe, accelerated the migration of photo-generated carriers, benefited electron storage, and effectively promoted the formation of C-C coupling intermediates for C<sub>2</sub>H<sub>4</sub>. For liquid products, the carbon nitride-supported Cu single-atom catalyst with a defective low-coordination Cu-N<sub>2</sub> motif (Cu-N<sub>2</sub>-V) exhibited superior photocatalytic activity for CO<sub>2</sub> reduction to ethanol relative to Cu-N<sub>3</sub> and Cu-N<sub>4</sub>.<sup>81</sup> In particular, Cu in Cu-N<sub>2</sub>-V existed in both Cu<sup>+</sup> and Cu<sup>2+</sup> valence states. On the one hand, the Cu<sup>+</sup> sites benefited CO<sub>2</sub> activation. On the other hand, the coexistence of Cu<sup>+</sup>/Cu<sup>2+</sup> sites contributed to the strong adsorption of \*CO and subsequent \*CO-\*CO dimerization. Finally, ethanol was ultimately produced from \*CO-\*CO, which underwent a series of hydrogenation processes.

The d-band center tuning strategy influences the carrier transportation and the adsorption of the reactant and intermediate to promote photocatalytic CO<sub>2</sub> conversion, which can

be achieved by incorporating MAS. Bulk doping of single Ni atoms in WO<sub>2.72</sub> (B-Ni<sub>1</sub>/WO<sub>2.72</sub>) displayed superior solar-driven CO<sub>2</sub> reduction performance to surface anchoring of single Ni atoms on WO<sub>2.72</sub> (S-Ni<sub>1</sub>/WO<sub>2.72</sub>).<sup>82</sup> The introduction of Ni atoms led to an upward shift of the d-band center of W atoms in the WO<sub>2.72</sub> host structure due to the overlapping orbital hybridization. Critically, the d-band center of W in B-Ni<sub>1</sub>/WO<sub>2.72</sub> shifted upward to a greater extent relative to S-Ni<sub>1</sub>/WO<sub>2.72</sub>. Therefore, the Ni atoms in B-Ni<sub>1</sub>/WO<sub>2.72</sub> exhibited stronger electronic interactions with the WO<sub>2.72</sub> host, facilitating the formation of charge-transfer channels that enabled the rapid transfer of photogenerated electrons to the surface Ni atoms. Moreover, the free energies of \*CO<sub>2</sub>, \*COOH, and \*CO intermediates of B-Ni<sub>1</sub>/WO<sub>2.72</sub> were integrally decreased compared to those on S-Ni<sub>1</sub>/WO<sub>2.72</sub>, benefiting the conversion of CO<sub>2</sub> to CO. Analogously, the decoration of isolated Mn atoms over the multi-edged TiO<sub>2</sub> nano-pompons shifted the d-band center upwards and pushed the antibonding orbital closer to the Fermi level, thus facilitating CO<sub>2</sub> adsorption.<sup>83</sup> The Mn site acted as an active center for CO<sub>2</sub> activation, and significantly reduced the formation energy barriers of \*COOH to accelerate the decisive step of the reaction.

Besides in-plane regulation, MAS can realize interlayer-spacing adjustment, which may significantly influence the carrier transport of the bulk-catalyst, thereby affecting CO<sub>2</sub> photoreduction. Single-atom In-bonded N-atom (In<sup>δ+</sup>-N<sub>4</sub>) in the (002) crystal planes of g-C<sub>3</sub>N<sub>4</sub> reduced the (002) interplanar spacing of g-C<sub>3</sub>N<sub>4</sub>, benefiting the separation of bulk carriers.<sup>84</sup> More charges were transferred to the adsorbed CO<sub>2</sub> molecule from the In<sup>δ+</sup>-N<sub>4</sub> active center (0.116 eV) compared to the bare C<sub>3</sub>N<sub>4</sub> site (0.006 eV), which was favorable for CO<sub>2</sub> adsorption. Moreover, the In<sup>δ+</sup>-N<sub>4</sub>-led CO<sub>2</sub> hydrogenation to \*COOH was downhill by -0.114 eV and evidently surpassed the uphill step by 2.09 eV on the bare C<sub>3</sub>N<sub>4</sub>, which optimized the reaction path.

### 3.2 Dual MAS

The precise construction of photocatalysts with dual MAS to achieve the simultaneous fostering of light absorption and catalytic activity is a formidable challenge. The bifunctional LaNi sites within COF were synthesized by electrostatically driven self-assembly approach.<sup>91</sup> The La-Ni dual MAS accelerated the dynamic behavior of the photogenerated charge carriers, comprising photoelectron transfer from La-Phen to the COF-5 colloid and subsequent electron injection into Ni-Phen for the CO<sub>2</sub> reduction process. In addition, the bimetallic LaNi coordination facilitated the generation of abundant \*COOH groups, and effectively decreased the activation barrier of CO<sub>2</sub> transformation. Moreover, the CO desorption was thermodynamically preferred over CHO\* formation, with an energy barrier of 0.72 eV *versus* 1.02 eV, resulting in high CO selectivity.

Precise control of the formation of Metal<sub>1</sub>···C=O···Metal<sub>2</sub> (M<sub>1</sub>···C=O···M<sub>2</sub>) intermediates at the photocatalyst interface is one of the critical steps in the formation of hydrocarbons. This is due to the fact that the energy required for simultaneous cleavage of the M<sub>1</sub>···O and M<sub>2</sub>···C bonds is much greater than that required for C-O bond breaking (Fig. 9a).<sup>92</sup> Ag<sub>2</sub>Cu<sub>2</sub>O<sub>3</sub>



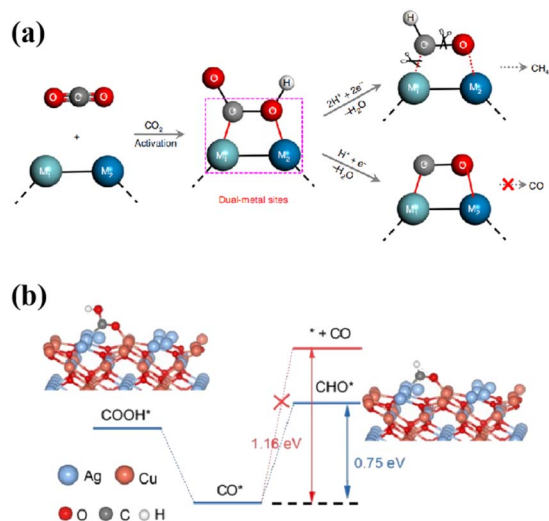


Fig. 9 (a)  $\text{CO}_2$  photoreduction into fuels such as  $\text{CH}_4$  and  $\text{CO}$  through the use of dual-metal-site catalytic systems ( $M$  represents the metal site, ' $\text{H}^+ + \text{e}^-$ ' refers to the proton coupled electron transfer process and ' $-\text{H}_2\text{O}$ ' means the desorption of  $\text{H}_2\text{O}$  molecules after the intermediates react with the proton–electron pair). This figure has been reproduced from ref. 92 with permission from Springer Nature, copyright 2019. (b) The rate-determined step of photoreduction of  $\text{CO}_2$  into  $\text{CH}_4$  over  $\text{Ag}_2\text{Cu}_2\text{O}_3$  nanowires. This figure has been reproduced from ref. 93 with permission from Wiley-VCH, copyright 2023.

nanowires with abundant Cu–Ag Lewis acid–base dual sites on the preferentially exposed (110) surface were utilized as a model catalyst to achieve 100% selectivity in the photogeneration of  $\text{CH}_4$  from  $\text{CO}_2$ .<sup>93</sup> The  $\text{Cu}\cdots\text{Ag}$  Lewis acid–base dual sites on  $\text{Ag}_2\text{Cu}_2\text{O}_3$ (110) regulated the  $\text{M}_1\cdots\text{C}=\text{O}\cdots\text{M}_2$  intermediate formation, converting  $\text{CO}_2$  into hydrocarbons. The rate-determining step with a corresponding Gibbs free energy ( $\Delta G(\text{CHO}^*)$ ) of 0.75 eV led to greater feasibility in  $\text{CO}^*$  forming  $\text{CHO}^*$  than desorbing from the catalyst surface (1.16 eV, Fig. 9b). Similarly, the highly stable Cu–C–O–In intermediate at the Cu–In dual sites of the sulfur-deficient  $\text{CuIn}_5\text{S}_8$  converted the endoergic protonation step to an exoergic reaction process, changing the reaction pathway to form  $\text{CH}_4$  instead of  $\text{CO}$ .<sup>92</sup> Furthermore, the  $\text{V}_\text{O}$ -regulated In–Ti dual sites enabled the formation of a stable adsorption conformation of the In–C–O–Ti intermediate, leading to the highly selective reduction of  $\text{CO}_2$  to  $\text{CH}_4$ .<sup>94</sup>

Catalysts containing dual MAS regulates the electron distribution by creating asymmetric atomic configurations, which significantly affects the photocatalytic performance, especially for multi-electron  $\text{CO}_2$  reduction. The mechanism of reverse electron transfer over Au and Co bimetallic atom catalysts was reported.<sup>95</sup> Electrons were delocalized from Au and accumulated around the Co atoms, resulting in the electron-rich Co atoms adsorbing/activating  $\text{CO}_2$  molecules readily, which significantly promoted photocatalytic  $\text{CO}_2$  reduction. In this regard, the Au/Co double single-atom loaded CdS increased the yield of  $\text{CO}$  and  $\text{CH}_4$  by nearly 2800% and 700%, respectively, compared to CdS alone. In addition, the disparate electron distributions and valence states of two distinct metal atoms

could endow significantly different charge distributions of the neighboring  $\text{C}_1$  intermediates to effectively suppress the electrostatic repulsion. The asymmetric Zn–O–Ge triatomic sites in the Vo-rich  $\text{Zn}_2\text{GeO}_4$  nanobelts induced distinct charge distributions of neighboring  $\text{C}_1$  intermediates, which facilitated the C–C coupling with a high  $\text{CO}_2$ -to- $\text{CH}_3\text{COOH}$  conversion rate of 29.95%.<sup>96</sup> Under similar mechanisms, incorporating redox-active  $\text{Co}^{2+}/\text{Ni}^{2+}$  cations (TM) into layered lead iodide hybrids (TJU-39(Pb)) achieved efficient photocatalytic  $\text{CO}_2$ -to- $\text{C}_2\text{H}_5\text{OH}$  conversion (yield of 24.9–31.4  $\mu\text{mol g}^{-1} \text{h}^{-1}$ , selectivity exceeding 90%).<sup>102</sup> It was experimentally demonstrated that the interlayer TMs were delocalized to the lead iodide layers to construct TM–O–Pd sites with substantial asymmetric charge distribution, which reduced the reaction barrier for C–C coupling. Specifically, the two-electron reduction of  $\text{CO}_2$  to  $\text{CO}^*$  occurred simultaneously at the charge-enriched  $\text{Pb}^{2+}$  sites and the  $\text{Ni}^{2+}$  site, which subsequently underwent C–C coupling to form  $\text{OC}-\text{CO}^*$  intermediates. The  $\text{OC}-\text{CO}^*$  intermediate coupled multiple  $\text{e}^-/\text{H}^+$  pairs, combining the dehydration process to finally yield  $\text{C}_2\text{H}_5\text{OH}$ .

From an overall reaction perspective, the  $\text{CO}_2$  photoreduction contains oxidation and reduction half-reactions, involving multiple proton-coupled electron transfer processes. The MAS construction not only enhances  $\text{CO}_2$  reduction, but also influences the corresponding oxidation half-reaction. The existence of an internal electric field pointing from the Ti cluster to the Cu cluster in MCOF- $\text{Ti}_6\text{Cu}_3$  facilitated carrier separation, leading to electron and hole transfer to the Cu cluster and Ti cluster, respectively.<sup>90</sup> Consequentially, electrons reaching the Cu cluster drove the reductive reactions, and the oxidative reaction proceeded at the Ti cluster. Analogously, two compatible active centers of Mn and Co were loaded onto carbon nitride ( $\text{Mn}_1\text{Co}_1/\text{CN}$ ).<sup>17</sup> The active center of Mn promoted  $\text{H}_2\text{O}$  oxidation by accumulating photogenerated holes, along with Co-facilitated  $\text{CO}_2$  activation by increasing the bond length and bond angle of  $\text{CO}_2$  molecules.

### 3.3 MAS combined with vacancies

Vacancies exhibit great influence on the properties of MAS. Vo-containing  $\text{Co}_3\text{O}_4$  hollow nanoparticles loaded on a macroporous N-doped carbon framework realized the photoreduction of low-concentration  $\text{CO}_2$  to  $\text{CO}$ .<sup>133</sup> Vo distorted the nearby Co–O bonds, broke the local structural symmetry of the Co–O–Co sites, and thus caused an asymmetric distribution of charge density compared with pristine  $\text{Co}_3\text{O}_4$ . This asymmetrical active site with a polarized electronic structure endowed a stronger electrostatic interaction between the  $\text{CO}_2$  molecule and Vo, which switched the  $\text{CO}_2$  configuration from a single-site linear model to a multiple-sites bending one, therefore facilitating  $\text{CO}_2$  activation. Moreover, the hydrogenation of adsorbed  $^*\text{CO}_2$  proceeded smoothly on the Vo- $\text{Co}_3\text{O}_4$  surface, and the adsorption capacity of  $^*\text{COOH}$  was obviously stronger than that of  $\text{Co}_3\text{O}_4$ . Mn dopants and Vo were engineered in  $\text{Zn}_2\text{GeO}_4$  nanorods (denoted as Mn-ZGO-Vo), which exhibited prominent photocatalytic  $\text{CO}_2$  reduction performance.<sup>105</sup> The introduction of Vo in Mn-ZGO-Vo caused the charge accumulation on the Mn





atoms near Vo, certainly favoring the electron-rich Mn sites for CO<sub>2</sub> molecule capture. The lattice strain and ligand effects caused by Mn doping and Vo engineering elevated the d-band centers, endowing less filling of the antibonding states and hence stronger binding strength of CO<sub>2</sub>. Moreover, the formation of COOH\* on the Mn-ZGO-Vo slab changed from endothermic to exothermic, and the rate-limiting step was tuned to CO\* formation with a lowest energy barrier among ZGO and Mn-ZGO. Precisely constructed Cu single-atom centers and two-coordinated N vacancies as dual active sites on carbon nitride (Cu<sub>1</sub>/N<sub>2</sub>CV-CN) achieved a high carbon-based selectivity of 98.50% for CO production.<sup>106</sup> The atomic Cu active sites promoted the chemisorption of CO<sub>2</sub> by changing the electronic structure of the surface. The N<sub>2</sub>C vacancy became the active site for the adsorption of H<sub>2</sub>O, which accelerated the dissociation of H<sub>2</sub>O by reducing the dissociation energy barrier of H<sub>2</sub>O from 2.59 eV to 1.68 eV. Moreover, the decrease in the rate-limiting step (the formation of COOH\* species) by the dual active sites in Cu<sub>1</sub>/N<sub>2</sub>CV-CN led to a decent CO production rate of 11.12 μmol g<sup>-1</sup> h<sup>-1</sup>.

The geometry of MAS regulated by vacancies ultimately affects the catalytic performance to generate C<sub>2+</sub>. Ultra-thin CuGaS<sub>2</sub>/Ga<sub>2</sub>S<sub>3</sub> containing Vs realized the selectivity of C<sub>2</sub>H<sub>4</sub>, reaching ≈ 93.87% with the yield of ≈ 335.67 μmol g<sup>-1</sup> h<sup>-1</sup>.<sup>107</sup> Vs induced a highly delocalized electron distribution in the original region of S atoms, forming a Cu–Ga metallic bond. The upshift of the d-band center of Cu–Ga ions induced by Vs could not only enforce the adsorption ability for the intermediates of \*CHOH\*CO to initiate C–C coupling, but also accumulate electrons to drive the kinetic process of photocatalytic CO<sub>2</sub> reduction.

### 3.4 MAS synergizing with nanoparticles

The synergistic effect of MAS and nanoparticle accelerates the complex activation and hydrogenation process of photocatalysis. Introducing such a complex structure for simultaneous CO<sub>2</sub> reduction and H<sub>2</sub>O dissociation is still a formidable challenge, and its underlying mechanism remains to be elucidated. The nitrogen-doped carbon anchoring with Cu nanoparticles and Ni single-atom sites (Ni<sub>1</sub>Cu<sub>NP</sub> N–C) were hybridized with CoAl-LDH (CA) for photocatalytic CO<sub>2</sub> reduction (CA/Ni<sub>1</sub>Cu<sub>NP</sub> N–C).<sup>109</sup> The photogenerated electrons of CoAl-LDH were transferred to N–C in the presence of the internal potential, and eventually accumulated on dispersed Ni single-atom sites. Meanwhile, the loading of Cu nanoparticles could significantly facilitate this charge transfer. The Ni center showed a high charge density, which facilitated reactant/intermediate adsorption and promoted catalytic reactions with multi-electron participation. Furthermore, the charge density around the electron-rich center Ni–N<sub>4</sub> showed an asymmetric distribution in the presence of Cu nanoparticles. This asymmetric active site was favorable for coupling adjacent \*CO, thus promoting the generation of C<sub>2</sub> products. A cooperative catalyst containing Ag nanoparticles with adjacent atomic cobalt–silver dual-metal sites on P-doped carbon nitride (Co<sub>1</sub>Ag<sub>(1+n)</sub>-PCN) was reported for photocatalytic CO<sub>2</sub>

reduction.<sup>110</sup> The asymmetric Co–N<sub>6</sub>–P sites coupled with Ag–N<sub>2</sub>C<sub>2</sub> sites could serve as the charge transfer channel to facilitate the migration of electrons to the surface reaction sites, while Ag nanoparticles acted as the electron acceptor to enrich and separate photogenerated electrons. Moreover, the synergistic function of Ag nanoparticles with adjacent atomically dispersed Ag–N<sub>2</sub>C<sub>2</sub> and Co–N<sub>6</sub>–P single-atom sites promoted the adsorption of CO<sub>2</sub> molecules onto the photocatalyst surface, and facilitated the formation of CO<sub>2</sub>\* and COOH\*.

### 3.5 MAS within a heterostructure

The construction of heterogeneous structures enhances light absorption and provides sufficient reaction sites.<sup>44</sup> In addition, the heterostructure can realize the spatial separation of the reduction and oxidation reaction sites, improving the utilization rate of the photogenerated carrier and preserving high-energy electrons and holes. MAS is conducive to the tight connection of heterogeneous structures and promotes the directional carrier transportation. The presence of Vo exposed Bi atoms on the Bi<sub>3</sub>O<sub>4</sub>Br surface, which formed an interfacial Bi–O bond by grafting the terminal O of the cobalt porphyrin (Co-TCPP).<sup>115</sup> The Bi–O bond, as a charge-transfer bridge, promoted the extraction and transfer of photogenerated electrons from the external [Bi<sub>3</sub>O<sub>4</sub>] layers to Co-TCPP. This contributed an effective space charge separation and the slow recombination process on the μs–ms time scale of CoTCPP. MoS<sub>2</sub> decorated with Cu species (Cu<sub>1</sub>/MS) was coated on the surface of MIL-125-NH<sub>2</sub> (MIL), which constructed a N–Cu<sub>1</sub>–S single-atom electron bridge (denoted as Cu-SAEB).<sup>116</sup> The Cu-SAEB achieved a Z-scheme charge-transfer mode between Cu<sub>1</sub>/MS and MIL, thus prolonging the lifetimes of carriers with a strong redox potential. Benefiting from the strengthened contact interface of Cu-SAEB, the highly active and stable CO<sub>2</sub> reduction performance was achieved, with CO and O<sub>2</sub> formation rates of 236.0 and 120.1 μmol g<sup>-1</sup> h<sup>-1</sup>, respectively. Similarly, an In–O–Cd bond-modulated S-scheme heterojunction of In<sub>2</sub>O<sub>3</sub>/CdSe-diethylenetriamine accelerated the photogenerated electron transfer.<sup>117</sup> Combined with the electron capture effect of Vo in In<sub>2</sub>O<sub>3</sub>, the In–Vo–In–O–Cd structural units at the interface led to the extraction of electrons and the rapid transfer to the surface-active sites, improving the electronic coupling of CO<sub>2</sub>.

The interface of the heterostructure could natively provide MAS for photocatalytic reactions. For example, the unique Cu–C and Cu–N dual chemical bond at the interface of the fabricated g-C<sub>3</sub>N<sub>4</sub>/Cu<sub>2</sub>SnS<sub>3</sub> nanocomposite led to a superior CO formation rate from CO<sub>2</sub> photoreduction.<sup>118</sup> The Z-scheme carrier conduction was highly activated due to the interfacial nitrogen vacancies *via* the Cu–C and Cu–N bonding for CO<sub>2</sub> reduction on the conduction band (CB) of Cu<sub>2</sub>SnS<sub>3</sub> and water oxidation on the VB of g-C<sub>3</sub>N<sub>4</sub>. The more negative overall free energy of Cu sites relative to Sn and S implied that the CO<sub>2</sub> conversion reaction occurred mainly *via* effective dual bonds between Cu sites and the C and N elements in g-C<sub>3</sub>N<sub>4</sub>.<sup>118</sup>

Heterogeneous structures enriched with MAS can generate C<sub>2+</sub> products. A novel supramolecular assembly of NiAl-Fe-TCPP obtained by intercalating iron porphyrin (Fe-TCPP) into



NiAl-layered double hydroxide (NiAl-LDH) exhibited superior catalytic performance of CO<sub>2</sub> photoreduction to derive C<sub>2</sub>H<sub>4</sub> with high selectivity up to 93.4%.<sup>119</sup> The strong host-guest interaction between LDH and Fe-TCPP led to the electron transfer from NiAl-LDH to Fe-TCPP. According to the *ex/in situ* XAS, the valence of Fe decreased along with the increase of Ni valence compared with that of Fe-TCPP and LDH, respectively. The low valence of Fe in NiAl-Fe-TCPP facilitated the CO\* hydrogenation and coupling with CHO\* to form COCHO\*. Particularly, the CO<sub>2</sub> activation to CO was accomplished on NiAl-LDH, and then spilled to Fe-TCPP and coupled to generate COCHO\*, which was further hydrogenated to produce C<sub>2</sub>H<sub>4</sub>. The O-In-P polarized sites at the r-In<sub>2</sub>O<sub>3</sub>/InP interface promoted C-C coupling with a productivity of 96.7 μmol g<sup>-1</sup> and selectivity >96% for CO<sub>2</sub> photoreduction to CH<sub>3</sub>COOH.<sup>120</sup> The interfacial In atoms accumulated electrons and transferred electrons to CO<sub>2</sub>, thus promoting CO<sub>2</sub> adsorption and activation. The quite different carbon Bader charges of OCCO\* on r-In<sub>2</sub>O<sub>3</sub>/InP caused by the formation of rich O-In-P reactive sites at the interface alleviated dipole-dipole repulsion and promoted C-C coupling (Fig. 10a-c). Ultimately, the C-C coupling energy barrier of r-In<sub>2</sub>O<sub>3</sub>/InP (0.5461 eV) was lower than that of pure In<sub>2</sub>O<sub>3</sub> (0.9446 eV), suggesting that the formation of heterostructures by modifying In<sub>2</sub>O<sub>3</sub> with P favored the formation of C<sub>2+</sub> products (Fig. 10d).

### 3.6 MAS as cocatalysts

The cocatalyst plays a crucial role in semiconductor-based photocatalysis, which is conducive to the migration of electrons or holes, and improves the utilization efficiency of the photogenerated carrier. Moreover, cocatalysts can reduce the activation energy and overpotential of the CO<sub>2</sub> conversion to speed up the surface reaction.<sup>44</sup> MAS used as cocatalysts can

effectively improve photocatalytic performance. Bi nanoclusters (NCs) were prepared *in situ* on Bi<sub>2</sub>O<sub>3</sub> through dehalogenation of Bi<sub>3</sub>O<sub>4</sub>Br by regulating the pH value in the hydrothermal process.<sup>122</sup> The construction of Bi sites on the basis of Bi<sub>2</sub>O<sub>3</sub> could promote photogenerated charge transfer through the Schottky junction. Moreover, the change of the valence state of Bi regulated the type of active sites from O of the original Bi<sub>2</sub>O<sub>3</sub> to Bi<sup>0</sup> of the Bi NCs in Bi NCs/Bi<sub>2</sub>O<sub>3</sub>, thus regulating the path of CO<sub>2</sub> photoreduction. Thermodynamically, the \*CO intermediate on the Bi site tended to hydrogenate to \*CHO species, accompanied by a subsequent multi-step hydrogenation process that selectively generated CH<sub>4</sub> on Bi NCs/Bi<sub>2</sub>O<sub>3</sub>. The \*CO desorption to form CO over Bi<sub>2</sub>O<sub>3</sub> was spontaneous and exothermic, whereas the hydrogenation of \*CO to form the \*CHO species required overcoming a large energy barrier (2.29 eV), leading to CO being the only reduction product of Bi<sub>2</sub>O<sub>3</sub>. Similarly, the CsCuCl<sub>3</sub>/Cu heterojunction synthesized *via* a simple acid-etching solution process exhibited high CH<sub>4</sub> selectivity.<sup>123</sup> The accumulating of charges at the contact interface between CsCuCl<sub>3</sub> and Cu nanocrystals formed a Schottky contact, facilitating the extraction of photoelectrons from CsCuCl<sub>3</sub> to Cu nanocrystals, thereby realizing the effective separation of photogenerated electron-hole pairs. Moreover, the Cu nanocrystals accelerated the photocatalytic CO<sub>2</sub> reduction toward CH<sub>4</sub> *via* manipulating the adsorption and activation of CO<sub>2</sub> and stabilizing the reaction intermediates.

The surface plasmon resonance of MAS plays a crucial role in the collection and conversion of solar energy by the strong local fields. The coexistences of Vo and Bi clusters generated *in situ* on ultrathin Bi<sub>12</sub>O<sub>17</sub>Cl<sub>2</sub> nanosheets contributed to the high efficiency of the CO<sub>2</sub>-to-CO conversion.<sup>124</sup> The Bi clusters exhibited a plasmon effect that extended the light absorption and enabled more sunlight harvest. Furthermore, Bi clusters acted as hole trapping centres in synergy with Vo as electron trapping sites, leading to the spatial separation of photo-generated electron-hole pairs. As another example, the attachment of non-noble plasmonic Bi particles with BiOCl shells to self-assembled TiO<sub>2</sub> nanosheets created a transformative hybrid plasmonic nanostructure. Bi stabilized by the BiOCl shell generated robust localized surface plasmon resonances, inducing a local field enhancement of 7–9 times, thus enabling the efficient and selective CO<sub>2</sub>-to-methanol conversion at the TiO<sub>2</sub>-BiOCl heterointerfaces.<sup>125</sup> In addition, it is worth mentioning that the localized surface plasmon resonance effect of Bi nanoparticles could significantly improve the rate and selectivity of the C<sub>2</sub>H<sub>5</sub>OH generation.<sup>132</sup> The high localized electron density and abundance of hot electrons in the active site drove the multi-electron reduction reaction, favoring the generation of C<sub>2+</sub> products.

Plasmon resonance-mediated photocatalysis on precious metal surfaces (mainly Ag and Au) shows great potential for solar energy harvesting and conversion. For instance, plasmonic Au mediated the S-scheme charge transfer, and generated additional energetic hot electrons and holes to inject to the CB of ZnIn<sub>2</sub>S<sub>4</sub> and VB of CuS, respectively, enabling a more thorough separation of carriers for CO<sub>2</sub> reduction and H<sub>2</sub>O oxidation.<sup>134</sup> Moreover, a new idea of plasmonic active “hot

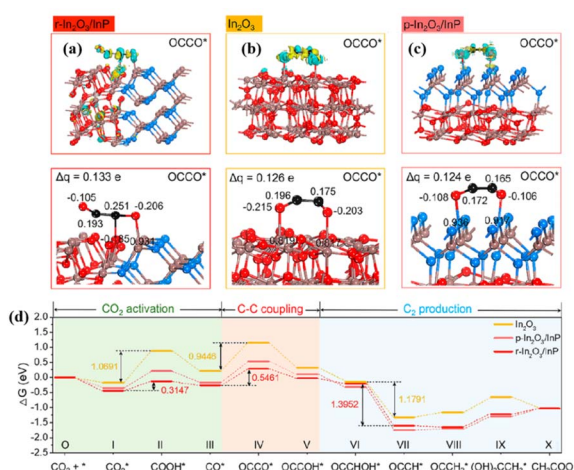


Fig. 10 Calculated electron density difference diagrams and the Bader charge values of (a) r-In<sub>2</sub>O<sub>3</sub>/InP, (b) In<sub>2</sub>O<sub>3</sub>, and (c) p-In<sub>2</sub>O<sub>3</sub>/InP with OCCO\* absorbed. (d) Free energy diagrams for the reduction of CO<sub>2</sub> to CH<sub>3</sub>COOH over r-In<sub>2</sub>O<sub>3</sub>/InP, In<sub>2</sub>O<sub>3</sub>, and p-In<sub>2</sub>O<sub>3</sub>/InP. These figures have been reproduced from ref. 120 with permission from American Chemical Society, copyright 2023.



spot"-confined photocatalysis was proposed to improve the photocatalytic CO<sub>2</sub> conversion. Specifically, tiny gaps (<10 nm) between the plasma nanostructures promoted plasma coupling between the nanostructures, resulting in the formation of classical "hot spots". The Au/TiO<sub>2</sub>/W<sub>18</sub>O<sub>49</sub> sandwich-like substructures with the short distance (<10 nm) between Au and adjacent W<sub>18</sub>O<sub>49</sub> induced an intense plasmon-coupling to form the active "hot spots" in the substructures.<sup>126</sup> These active "hot spots" could gather the incident light to enhance "hot electron" generation and migration, and capture protons and \*CO through the dual-hetero-active-sites (Au–O–Ti and W–O–Ti) at the Au/TiO<sub>2</sub>/W<sub>18</sub>O<sub>49</sub> interface, thus accelerating the protonation of \*CO intermediates to derive CH<sub>4</sub>.

Alloys as MAS enhance light absorption, inhibit charge recombination, and adsorb and activate reactants, thereby improving the selectivity of specific products. The PtAg alloy over HNb<sub>3</sub>O<sub>8</sub> nanosheets trapped the electrons and improved the charge separation efficiency, mitigating the kinetical challenge of the eight-electron transfer process for CH<sub>4</sub>.<sup>127</sup> In addition, the PtAg alloy acted as synergistic sites to reduce CO<sub>2</sub> to CO intermediates at the Ag site, which were then spilled over or sequentially adsorbed at neighboring Pt sites for further hydrogenation to CH<sub>4</sub>. As another example, PtCu alloys with appropriate Pt/Cu ratios were deposited onto TiO<sub>2</sub> nanocrystals, which significantly improved CH<sub>4</sub> production with 100% selectivity.<sup>128</sup> The PtCu alloy effectively facilitated the separation/transfer of photogenerated charges, benefited the adsorption of CO<sub>2</sub>, and promoted the formation and activation of intermediates (CO<sub>2</sub><sup>-</sup>, \*COOH, \*CO, and \*CHO). The synergistic effect of PtCu lowered the activation energy barriers of \*CO<sub>2</sub> and \*CHO, inhibited the desorption of \*CO, and ultimately optimized the efficiency and selectivity of CH<sub>4</sub>.

The alloy MAS promotes the C–C coupling and desorption of \*C<sub>2</sub> intermediates from the catalyst surface. Loading Cu–Ag alloy sub-nanoclusters (ASNCs) on TiO<sub>2</sub> for CO<sub>2</sub> photoreduction produced C<sub>2</sub>H<sub>4</sub> with a record-high formation rate (1110.6 ± 82.5 μmol g<sup>-1</sup> h<sup>-1</sup>).<sup>129</sup> The interaction between Cu and Ag in the Cu–Ag ASNCs promoted the C–C coupling of CH<sub>2</sub>\* at the Cu active site, which led to the spontaneous formation of \*C<sub>2</sub>H<sub>4</sub> from CH<sub>2</sub>\* on Cu–Ag alloy/TiO<sub>2</sub>. In addition, the desorption energy of \*C<sub>2</sub>H<sub>4</sub> in the Cu–Ag alloy/TiO<sub>2</sub> was lower than that in Ag/TiO<sub>2</sub>. This suggested that the interaction between Cu and Ag promoted the desorption of \*C<sub>2</sub>H<sub>4</sub>, and thus the selective and efficient production of C<sub>2</sub>H<sub>4</sub>. Ag, in conjunction with Ir, achieved C–C coupling by inserting CO<sub>2</sub> into –CH<sub>3</sub>, facilitating the formation of C<sub>2</sub>\*, during CO<sub>2</sub> photoreduction.<sup>130</sup> Specifically, the assembly of AuIr with InGa<sub>3</sub>N nanowires on silicon achieved a C<sub>2</sub>H<sub>6</sub> activity of 58.8 mmol g<sup>-1</sup> h<sup>-1</sup> with a turnover number of 54 595 over 60 h. The Ir sites in Au–Ir alloys increased CO<sub>2</sub> reduction activity by lowering the reaction energy of key elementary steps (for example, CO<sub>2</sub> to \*COOH on pure Au and \*CO to \*CHO on Au<sub>3</sub>Ir<sub>1</sub> alloy) and steered the selectivity from the dominant HER to C–C coupling. The insertion of CO<sub>2</sub> into \*CH<sub>3</sub> toward \*CH<sub>3</sub>COO exhibited the lowest reaction energy compared with other C–C coupling forms (CH + \*CH → \*C<sub>2</sub>H<sub>2</sub>, \*CH<sub>2</sub> + \*CH<sub>2</sub> → \*C<sub>2</sub>H<sub>4</sub>, \*CH<sub>3</sub> + \*CH<sub>3</sub> → C<sub>2</sub>H<sub>6</sub>(g) and CO<sub>2</sub>

insertion into \*CH<sub>3</sub> to \*CH<sub>3</sub>COO), revealing the possible mechanism of C–C coupling for C<sub>2</sub>H<sub>6</sub> synthesis.

## 4 Identification the role of MAS in photocatalysis

With the growing development in nanoscale characterization, a variety of techniques have emerged to assess the role played by MAS in photocatalysis. Specifically, microscopic visual characterization combined with spectroscopic measurements can help to reveal the structure and the coordination environments of the sample, along with the *in situ* observation of intermediary transformations to profoundly reveal the reaction mechanisms. In addition, theoretical calculations simulating the role of MAS in photocatalysis reveal the physical and chemical properties exhibited by MAS during CO<sub>2</sub> conversion.<sup>135</sup>

### 4.1 High-resolution aberration-corrected high-angle annular dark-field scanning transmission electron microscopy (AC-HAADF-STEM)

In the structural characterization of single-atom catalysts, high-resolution AC-HAADF-STEM demonstrates paramount importance in elucidating the distribution of the MAS and its geometry. Isolated Co single-atom-modified 2D monolayer ZIS nanosheet composites (Co-<sup>s</sup>ZIS) possessed dual active centers of Co and Zn.<sup>136</sup> AC-HAADF-STEM was used to characterize the dispersion and configuration of the atoms involved, and to assist in determining the atomic structure of Co-<sup>s</sup>ZIS. Fig. 11a clearly shows the distribution of isolated Co atoms in <sup>s</sup>ZIS, with the yellow circles marking the atomic spots that were brighter compared to the surrounding support. Fig. 11b and c reflects the fact that the corresponding atoms exhibited different

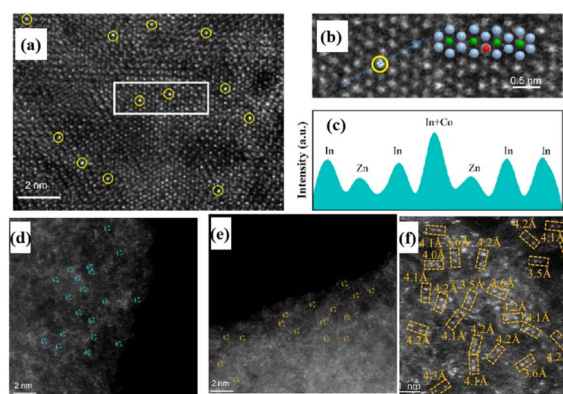


Fig. 11 (a) Aberration-corrected HAADF STEM image of the Co-<sup>s</sup>ZIS; single-atomic Co sites are highlighted by yellow circles. (b) Magnified view of the white box in (a) (inset is the simulated atom distribution of Co-<sup>s</sup>ZIS, and the green, gray, and red spheres represent the Zn, In, and Co atoms, respectively). (c) Intensity profile corresponding to the dark cyan arrow in (b). These figures have been reproduced from ref. 136 with permission from American Chemical Society, copyright 2023. Aberration-corrected HAADF-STEM images of (d) Ni–N–C, (e) Fe–N–C, and (f) (Ni, Fe)–N–C. These figures have been reproduced from ref. 137 with permission from Wiley–VCH, copyright 2023.





contrasts, with one of the largest peaks corresponding to the overlapping intensity spectra of an In atom and the individual Co atom. In addition, AC-HAADF-STEM was used to further examine the detailed distribution state of the MAS. The bright spots in Fig. 11d and e confirmed the isolated dispersion of Ni or Fe atoms on the carbon skeleton of the Ni–N–C and Fe–N–C single-atom catalysts, respectively, and no atom pairs were observed. In contrast, the AC-HAADF-STEM images of the (Ni, Fe) dual-single-atom catalysts (Fig. 11f) clearly showed most of the bright spots appearing in pairs, marked by yellow rectangles, confirming the formation of Ni/Fe dual-atom pairs with an average distance of about 4.1 Å.<sup>137</sup>

## 4.2 X-ray photoelectron spectroscopy (XPS)

XPS is considered to be an effective method to analyze the surface properties of the catalysts, reflecting the chemical bonding composition and the migration paths of carriers based on peak shifts. Porous covalent triazine frameworks (CTFs) were combined with CdS nanorods to obtain CdS@CTF-HUST-1 heterojunction photocatalysts with core-shell structures for CO<sub>2</sub>-to-CO conversion.<sup>138</sup> Essentially, the full XPS spectra showed the coexistence of Cd, S, C and N elements in the CdS@CTF-HUST-1 with an optimal CdS content, referred to as Cd(0.9)@CTF. *In situ* XPS was conducive to revealing S-scheme charge transfer mechanisms of CdS@CTF-HUST-1. As shown in Fig. 12, the Cd 3d and S 2p peaks of the CdS(0.9)@CTF sample showed a positive displacement with respect to CdS, while the C 1s and N 1s peaks of CdS(0.9)@CTF exhibited a negative shift relative to CTF-HUST-1 under dark conditions. Such shifts indicated the interfacial transfer pathway of electrons from CdS to CTF-HUST-1. Under light illumination, the binding energies of Cd 3d and S 2p of the CdS(0.9)@CTF were negatively shifted compared to those in darkness, while the binding energies of C 1s and N 1s underwent positive

displacement. These peak shifts confirmed that the internal electric field could drive the transfer of photogenerated electrons from CTF-HUST-1 to CdS under light irradiation. Furthermore, *in situ* irradiated XPS validated the Z-scheme charge transfer path of Ni-doped CsPbBr<sub>3</sub>/Bi<sub>3</sub>O<sub>4</sub>Br with an internal electric field directing from Ni-doped CsPbBr<sub>3</sub> to Bi<sub>3</sub>O<sub>4</sub>Br.<sup>114</sup> The binding energies of Cs, Pb and Br of CsPbBr<sub>3</sub> were all positively shifted upon Ni doping, suggesting that the introduced Ni sites interacted with the surrounding atoms to reduce the electron density around the Cs, Pb and Br atoms. After composing the heterostructure, the Cs 3d and Pb 4f of Ni-doped CsPbBr<sub>3</sub>/Bi<sub>3</sub>O<sub>4</sub>Br were shifted to higher binding energy by 0.3 eV with respect to Ni-doped CsPbBr<sub>3</sub>, whereas Bi 4f and O 1s underwent a 0.2 eV shift to lower binding energy with respect to Bi<sub>3</sub>O<sub>4</sub>Br. In addition, the distance between the Br 3d<sub>5/2</sub> and Br 3d<sub>3/2</sub> peaks increased, indicating an enhanced spin-orbit splitting function of Br 3d. These results revealed changes in the charge loss and accumulation states of Ni-doped CsPbBr<sub>3</sub> and Bi<sub>3</sub>O<sub>4</sub>Br in the heterostructures, demonstrating the strong interfacial interaction between Bi<sub>3</sub>O<sub>4</sub>Br and Ni-doped CsPbBr<sub>3</sub>. Upon illumination, Cs 3d and Pb 4f moved toward lower binding energies relative to the characteristic peaks in the dark environment, while Bi 4f and O 1s exhibited significant positive shifts. These results suggested that the light-induced electrons follow a Z-scheme path from Bi<sub>3</sub>O<sub>4</sub>Br to Ni-doped CsPbBr<sub>3</sub>.

## 4.3 X-ray absorption fine structure (XAFS)

Based on synchrotron radiation, XAFS has become an important technique to reveal the electronic structure, coordination number and bonding environment of MAS, and is widely used to study MAS-containing catalytic systems. Specifically, the technique is usually classified into X-ray absorption near-edge structure (XANES) and extended X-ray absorption fine structure (EXAFS).<sup>139</sup>

Cu–N<sub>4</sub> sites-anchored phosphorus-modulated carbon nitride (CuACs/PCN) regulated the intermediate energy levels to achieve C<sub>2</sub>H<sub>4</sub> formation during CO<sub>2</sub> photoreduction.<sup>85</sup> The Cu K-edge XANES of CuACs/PCN was between Cu<sub>2</sub>O and CuO (Fig. 13a), indicating that the oxidation state of Cu is between +1 and +2. In the EXAFS spectrum (Fig. 13b), CuACs/PCN had a prominent peak near 1.5 Å, corresponding to the scattering of the Cu–N bond in the first coordination shell. The absence of the Cu–Cu coordination (2.2 Å) indicated that the Cu sites were atomically dispersed. From the fitting results (Fig. 13c), Cu atoms in CuACs/PCN were coordinated by four N atoms at a distance of 1.97 Å. The wavelet transform contour plot of CuACs/PCN exhibited a radial distance of 1.5 Å (Y-axis), which was significantly different from that of the Cu foil. These results strongly demonstrated that Cu atoms were dispersed with Cu–N<sub>4</sub> coordination in CuACs/PCN. In addition, XAFS was applied to study the coordination environment of MAS in Co<sub>1</sub>Ag<sub>(1+n)</sub>-PCN.<sup>110</sup> In the Ag K-edge XANES spectra, the near-edge absorption peak of Co<sub>1</sub>Ag<sub>(1+n)</sub>PCN was located above Ag<sub>2</sub>O, indicating that the valence state of Ag was near +1 (Fig. 13e). Two main peaks at 1.5 and 2.4 Å in the Fourier-transformed Ag k<sup>2</sup>-weighted EXAFS spectra (Fig. 13f) corresponded to the first

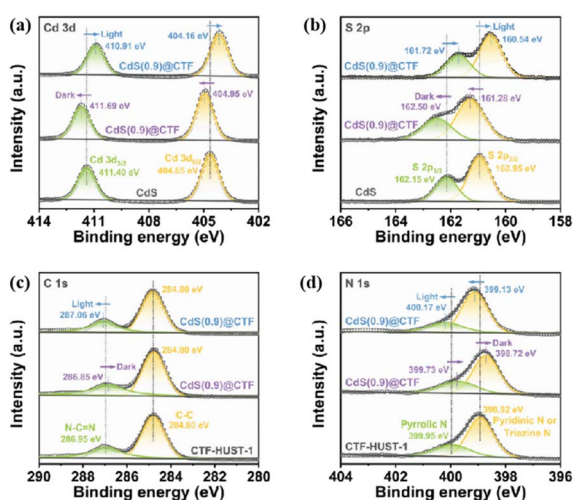


Fig. 12 High-resolution XPS spectra of (a) Cd 3d, (b) S 2p, (c) C 1s, and (d) N 1s of CdS, CTF-HUST-1, and CdS(0.9)@CTF samples. The *in situ* XPS measurement was performed under light irradiation. These figures have been reproduced from ref. 138 with permission from Wiley-VCH, copyright 2023.





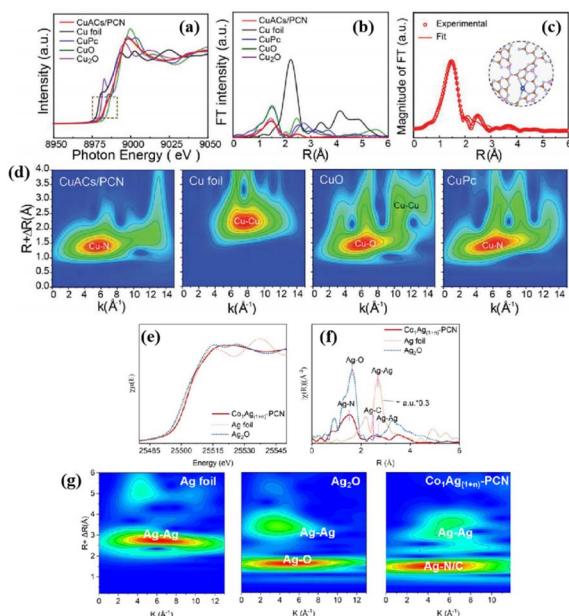


Fig. 13 (a) XANES and (b) EXAFS spectra of the Cu K-edge of CuACs/PCN, Cu foil, Cu<sub>2</sub>O, CuO, and CuPc. (c) The EXAFS fitting curves of CuACs/PCN at *R*-space. (d) WT EXAFS of the Cu K-edge. These figures have been reproduced from ref. 85 with permission from Wiley-VCH, copyright 2022. Ag K-edge (e) XANES, (f) EXAFS, and (g) WT-EXAFS spectra of Co<sub>1</sub>Ag<sub>(1+n)</sub>-PCN. These figures have been reproduced from ref. 110 with permission from American Chemical Society, copyright 2023.

shell layer of Ag–N and the second shell layer of Ag–C, respectively. The presence of Ag–Ag coordination (2.6 Å) indicated that Ag existed in the form of single atoms and nanoparticles. The wavelet transform Ag K-edge EXAFS of Co<sub>1</sub>Ag<sub>(1+n)</sub>PCN showed a maximum peak around 4.7 Å, which was different from that of the Ag foil and Ag<sub>2</sub>O, attributed to Ag–N/C coordination. Specifically, the EXAFS fitting of the shell coordination elucidated that the Ag atom was coordinated to 2.3 N atoms and 1.7C atoms, referred as the Ag–N<sub>2</sub>C<sub>2</sub> site. Based on a similar analytical procedure, the existence of a Co–N<sub>6</sub>–P configuration of the Co single atom in Co<sub>1</sub>Ag<sub>(1+n)</sub>PCN was also revealed.

#### 4.4 Diffuse reflectance infrared Fourier-transformed spectroscopy (DRIFTS)

DRIFTS can be used to deduce the structure of the compound, reflecting the type of functional groups contained in the substance. Characterization of intermediates generated on the catalyst surface using *in situ* DRIFTS provides support for the reaction pathway revelation and MAS identification. *In situ* DRIFTS was used to probe the reaction intermediates in the CO<sub>2</sub> photoreduction of Er-doped ZnIn<sub>2</sub>S<sub>4</sub>.<sup>86</sup> Under dark conditions, Er-doped ZnIn<sub>2</sub>S<sub>4</sub> exhibited distinct absorption peaks corresponding to monodentate carbonate (m-CO<sub>3</sub>) and bidentate carbonate (b-CO<sub>3</sub>), indicating the effective adsorption and activation of CO<sub>2</sub> and H<sub>2</sub>O. Under light conditions, the peaks of \*CHO (962 cm<sup>-1</sup>), \*OCH<sub>3</sub> (1043 cm<sup>-1</sup>) and \*COOH (1530 cm<sup>-1</sup>) appeared in Er-ZnIn<sub>2</sub>S<sub>4</sub>, which were the key intermediates for the subsequent generation of CH<sub>4</sub>. Both Er-ZnIn<sub>2</sub>S<sub>4</sub> and pure

ZnIn<sub>2</sub>S<sub>4</sub> showed absorption peaks for the \*CH<sub>2</sub> group at 2856 and 2935 cm<sup>-1</sup>, respectively, reflecting their tendency to generate CH<sub>4</sub>. Compared to pure ZnIn<sub>2</sub>S<sub>4</sub>, the Er-ZnIn<sub>2</sub>S<sub>4</sub> exhibited stronger b-CO<sub>3</sub> dissipation with stronger CO<sub>2</sub> reduction capacity. The spectrum of Er-ZnIn<sub>2</sub>S<sub>4</sub> had additional \*OCH<sub>2</sub> peaks between 1210–1240 cm<sup>-1</sup>, reflecting different CO<sub>2</sub> reduction pathways between Er-ZnIn<sub>2</sub>S<sub>4</sub> and ZnIn<sub>2</sub>S<sub>4</sub> (Er-ZnIn<sub>2</sub>S<sub>4</sub>: CO<sub>2</sub> → \*COOH → \*CO → \*CHO → \*OCH<sub>2</sub> → \*OCH<sub>3</sub> → CH<sub>4</sub>; ZnIn<sub>2</sub>S<sub>4</sub>: CO<sub>2</sub> → \*COOH → \*CO → \*CHO → \*CH<sub>2</sub>O → \*CH → \*CH<sub>2</sub> → \*CH<sub>3</sub> → CH<sub>4</sub>).

*In situ* DRIFTS identifies key intermediates of the C<sub>2+</sub> product, contributing to the inference of C–C coupling processes. In this regard, crucial C<sub>2</sub> intermediates including COCO\* (1374 and 1486 cm<sup>-1</sup>) and COCOH\* (1233 and 1574 cm<sup>-1</sup>) were observed on the Au–CeO<sub>2</sub> nanocomposite, providing strong evidence that the Au–O–Ce sites drove the generation of C<sub>2</sub>H<sub>6</sub> from the C–C coupling.<sup>97</sup> In addition, the peaks at 1367 and 1485 cm<sup>-1</sup> appearing in the In<sub>2</sub>O<sub>3</sub>/InP heterojunction were related to OCCO\*, a key intermediate in the generation of CH<sub>3</sub>COOH.<sup>120</sup> The peak at 1332 cm<sup>-1</sup> belonged to the C–H vibration of the hydrogenated intermediate after C–C coupling, and the peak at 1433 cm<sup>-1</sup> belonged to the COO stretching vibration of CH<sub>3</sub>COOH, further reflecting the generation of C<sub>2+</sub>.

#### 4.5 Raman

Raman spectroscopy identifies chemical bonds and functional groups. *In situ* Raman spectra can reveal the structural evolution of catalysts during catalytic reactions. For Vo-rich Zn<sub>2</sub>GeO<sub>4</sub>, CO<sub>2</sub> adsorption on Ge and Zn atoms gradually shifted the peak positions of the Zn–O–Ge stretching vibrations (~730 cm<sup>-1</sup>) and Zn–O–Ge bending vibrations (~785 cm<sup>-1</sup>) to higher wave numbers.<sup>96</sup> The Raman peak blue shift revealed the transfer of the electron cloud from the lattice oxygen to the metal atoms. The Zn–O–Ge stretching and Zn–O–Ge bending vibration peaks were again shifted to higher frequencies during CO<sub>2</sub> photoreduction, indicating that the electron cloud in the O 2p orbitals of the lattice oxygen was further transferred to the nearby Zn 4s or Ge 4s empty orbitals. This process provided electrons for the reduction of adsorbed CO<sub>2</sub> molecules and reaction intermediates. *In situ* Raman enables the real-time monitoring of the intermediate generation and conversion processes on the catalyst surface, revealing the reaction mechanism. In the *in situ* Raman spectrum, the peak before 500 cm<sup>-1</sup> was related to the structural properties of r-In<sub>2</sub>O<sub>3</sub>/InP.<sup>120</sup> With increasing light duration, the peak at 887 cm<sup>-1</sup> was designated as C–C–O stretching, reflecting the critical C–C coupling process for CH<sub>3</sub>COOH generation. The C≡O stretching vibration of CO\* (2909 cm<sup>-1</sup>) further validated that the CO\* coupling produced CH<sub>3</sub>COOH.

#### 4.6 Electrochemical analysis

Electrochemical analysis is widely used to reveal the kinetic processes of the migration and separation of photogenerated carriers in photocatalysis. Among them, transient photocurrent response and electrochemical impedance measurement (EIS)



are the most representative and widely used methods.<sup>140–144</sup> For example, the Cu–N<sub>4</sub> sites-anchored phosphorus-modulated carbon nitride (CuACs/PCN) exhibited the strongest photocurrent response relative to carbon nitride (CN), CuACs-anchored carbon nitride (CuACs/CN), and CuACs/PCNs with different P doping contents, reflecting its superior interfacial charge separation efficiency.<sup>85</sup> Moreover, EIS also demonstrated the lowest resistance of CuACs/PCN, thus confirming the efficient separation of photoexcited electron–hole pairs.

As another crucial feature, electrochemical analysis contributes to reveal the change of activation and reduction energy of CO<sub>2</sub> conversion. Kang's research group examined the Tafel plots of pure Cu, Cu/PVP and Cu/rGO/PVP/Nafion composite electrodes to estimate the reaction overpotentials of the samples.<sup>145</sup> The overpotentials of Cu/PVP (6.16 kJ mol<sup>-1</sup>) and Cu/rGO/PVP/Nafion (9.00 kJ mol<sup>-1</sup>) electrodes were significantly lower than those of the pure Cu electrode, revealing a decrease in the CO<sub>2</sub> reduction energy.

In addition, the Mott–Schottky measurement can be used to specify the semiconductor type and determine the valence band maximum (VBM) and conduction band minimum (CBM) potentials. For example, according to the results of the Mott–Schottky test, the Zr/Ti bimetallic oxide solid solution integrated with Au nanoparticles (Au/TZO) exhibited the characteristics of n-type semiconductors.<sup>131</sup> As the CBM of Au/TZO was estimated as –0.80 V with respect to a normal hydrogen electrode (NHE), the photocatalytic conversion of CO<sub>2</sub> to CO (–0.53 vs. NHE), CH<sub>4</sub> (–0.24 vs. NHE), C<sub>2</sub>H<sub>4</sub> (–0.34 vs. NHE) and C<sub>2</sub>H<sub>6</sub> (–0.27 vs. NHE) was thermodynamically feasible over Au/TZO. It is also worth mentioning that the electrochemical active surface area (ECSA) can be used to reveal the number of catalytically active sites. A larger ECSA indicates more active sites, which is more favorable for photocatalytic CO<sub>2</sub> conversion.<sup>146</sup>

#### 4.7 Theoretical calculations

Theoretical calculations can be used to obtain the atomic and electronic structures of the MAS, the adsorption strength of the intermediates, and the optimal reaction path.

Electronic property analysis can infer underlying factors affecting the catalytic activity. The d-band centers of Cu in Cu<sub>1</sub>N<sub>3</sub>@P(1)CN, Cu<sub>1</sub>N<sub>3</sub>@CN, and Cu<sub>1</sub>P<sub>3</sub>@PCN were determined to be –1.24 eV, –1.46 eV, and 11.60 eV, respectively, by partial density of states analysis, which depended on the local coordination environment of Cu.<sup>87</sup> As the d-band center of Cu approached the Fermi energy level, the catalytic activity for the COOH\* formation became higher. It is worth mentioning that the overlap between Cu 3d and P 3p in Cu<sub>1</sub>N<sub>3</sub>@P(1)CN was more pronounced than the overlap of Cu 3d with C 2p at the same corner position in Cu<sub>1</sub>N<sub>3</sub>@CN. This reflected the more pronounced orbital and electronic interactions of Cu and P in Cu<sub>1</sub>N<sub>3</sub>@P(1)CN than that of Cu and C in Cu<sub>1</sub>N<sub>3</sub>@CN, which moved the d-band center of Cu<sub>1</sub>N<sub>3</sub>@PCN closer to the Fermi energy level. Charge density difference analysis further demonstrated that the electronic interaction between Cu and COOH\* in Cu<sub>1</sub>N<sub>3</sub>@P(1)CN was the strongest relative to Cu<sub>1</sub>N<sub>3</sub>@CN and Cu<sub>1</sub>P<sub>3</sub>@PCN, prompting a large number of

electrons to be transferred from the Cu center to COOH\* in Cu<sub>1</sub>N<sub>3</sub>@P(1)CN, benefiting CO<sub>2</sub> activation.

Theoretical calculations provide insight into the mechanism of the photocatalytic CO<sub>2</sub> reduction reaction. From the free energy analysis, the introduction of Ag single atoms on hollow porous polygonal C<sub>3</sub>N<sub>4</sub> nanotubes (Ag<sub>1</sub>@PCNT) significantly enhanced the adsorption of \*CO<sub>2</sub> and weakened the adsorption of \*H, suggesting that Ag<sub>1</sub>@PCNT was more favorable for CO<sub>2</sub> conversion than for hydrogen production.<sup>88</sup> The COOH\* formation energy (the rate-limiting step) of Ag<sub>1</sub>@PCNT was lower than that of C<sub>3</sub>N<sub>4</sub> nanotubes. This suggests that the strong interaction of the Ag–N<sub>3</sub> coordination with \*COOH stabilized the \*COOH intermediate and reduced the barrier for CO<sub>2</sub> photoreduction (Fig. 14a and b). In addition, the generation of CO molecules by desorption of \*CO groups on the surface of Ag<sub>1</sub>@PCNT had a smaller Gibbs free energy than the protonation of \*CO into \*CHO, which contributed to the highly selective generation of CO.

Theoretical calculations can reveal the specific processes involved in the generation of C<sub>2+</sub> products, especially for C–C coupling. Calculation of the Gibbs free energy diagrams for CO<sub>2</sub> photoreduction on In and/or Cu-anchored poly-CN (InCu/poly-CN, Cu/poly-CN, and In/poly-CN) (Fig. 14c) revealed that the formation of \*COOH was a rate-determining step on InCu/poly-CN ( $\Delta G = +1.20$  eV) and In/poly-CN ( $\Delta G = +1.86$  eV), while the generation of \*COCH<sub>2</sub>OH was a rate-determining step on Cu/poly-CN ( $\Delta G = +1.98$  eV).<sup>98</sup> On InCu/poly-CN, \*CO underwent a dimerization reaction ( $\Delta G = 0.45$  eV) and a subsequent hydrogenation–electron addition process to ultimately generate CH<sub>3</sub>CH<sub>2</sub>OH. In the Cu/poly-CN system, \*CO was also coupled to form \*COCO, but its Gibbs free energy was higher than that of the InCu/poly-CN. Furthermore, the process from \*COCHOH to \*COCH<sub>2</sub>OH in Cu/poly-CN was endothermic with the highest gain ( $\Delta G = +1.98$  eV), resulting in lower CH<sub>3</sub>CH<sub>2</sub>OH yields for Cu/poly-CN relative to InCu/poly-CN. However, the \*CO

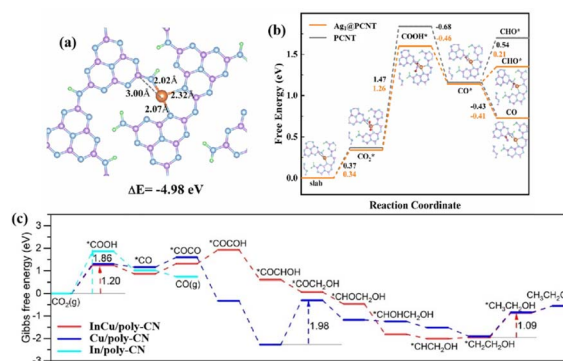


Fig. 14 (a) Structure of Ag<sub>1</sub>@PCNT. (b) Gibbs free energies of the CO<sub>2</sub> photoreduction pathways by DFT calculations over the Ag<sub>1</sub>@PCNT (Ag sites) and PCNT surfaces. Atom key: N (blue), C (purple), H (green), and Ag (orange). These figures have been reproduced from ref. 88 with permission from Wiley-VCH, copyright 2023. Gibbs free energy diagrams and CO<sub>2</sub>-to-ethanol photoreduction pathways on InCu/poly-CN, Cu/poly-CN, and In/poly-CN (c). This figure has been reproduced from ref. 98 with permission from Wiley-VCH, copyright 2022.



intermediates on In/poly-CN preferred desorption as CO products (exothermic) rather than C–C coupling, resulting in a poor  $\text{CH}_3\text{CH}_2\text{OH}$  yield on In/poly-CN.

## 5 Conclusion and perspectives

The photocatalysts containing MAS have been proved as efficient systems for converting incident solar energy into chemical fuel. In this review, typical photocatalytic materials containing MAS have been briefly introduced with clear examples. Then, the different roles of MAS in various forms in the photocatalytic  $\text{CO}_2$  reduction from the perspective of principles and applications are discussed in detail, greatly accelerating the surface charge separation/transfer, and enhancing the adsorption and activation of  $\text{CO}_2$ . Finally, advanced characterization techniques and theoretical calculation for revealing the function played by MAS in  $\text{CO}_2$  photoreduction are presented. Although considerable progress has been made in MAS-containing photocatalytic systems, there are still great challenges in practical applications that need to be further explored.

(1) The complexity of the preparation process and the difficulty of achieving uniform high-volume production are the major drawbacks of MAS-containing catalysts. In addition, the exposed MAS are susceptible to oxidation, resulting in performance degradation. Therefore, effective technologies should be continuously developed for the large-scale production of MAS-containing photocatalysts with stable and controllable surface states. Elaborate design strategies to improve the catalyst stability (*e.g.*, surface encapsulation and ligand grafting) need to be further explored. Continuous optimization of existing synthesis methods is an effective and viable solution.

(2) Although photocatalysts containing MAS have shown great potential in artificial photosynthesis, their performance is still unsatisfactory for practical production. Particularly, photocatalytic  $\text{CO}_2$  conversion involves a variety of intermediates and products, making it difficult to regulate the selectivity of the target product. For photocatalytic systems with MAS, the interactions of reactants and intermediates with the MAS affect the activation and conversion of  $\text{CO}_2$ , as well as C–C coupling. Defect design, doping, construction of heterostructures, and introduction of co-catalysts have become widely used strategies to enhance the  $\text{CO}_2$  photoreduction performance. However, there is still a need to continuously explore effective and novel strategies to improve the performance for real-world production, which remains elusive at the present stage.

(3) Accurate characterization and in-depth understanding of the mechanism of MAS in photocatalysis still face great challenges. It is crucial to carefully reveal the coordination environments of the MAS and its changes during the photocatalytic reaction. Specifically, the working mechanism of MAS in photocatalysis can be explored in-depth by advanced *in situ* characterisation techniques and accurate theoretical calculations, which guide the rational design and regulation of photocatalysts. Therefore, there is a need for the continuous development of highly sophisticated characterisation techniques, and theoretical computational models close to the actual reaction processes.

(4) In the face of the explosion of research data, the traditional research method of relying on pre-investigation to identify scientific problems has become overwhelming. This approach is costly, time-consuming, and increasingly difficult to meet the research needs of modern materials science. Nowadays, machine learning is changing the traditional research paradigm and bringing new opportunities for the development of related technologies and industrial upgrading. Combining machine learning techniques with the design of photocatalytic systems to rapidly mine effective information from a large amount of data is conducive to the construction of novel materials and the excavation of reaction mechanisms. Specifically, machine learning techniques are becoming a powerful tool for scientific research in the design and construction of photocatalysts, as well as in the prediction of physicochemical properties and mechanisms.

In summary, through continuous exploration and in-depth research, it is found that photocatalytic  $\text{CO}_2$  reduction technology is expected to realize the establishment of a resource-saving and environmentally-friendly energy system, and improve human life in the near future.

## Data availability

No primary research results, software or code have been included and no new data were generated or analysed as part of this review.

## Author contributions

All authors participated in this review work. W. Gao, Y. Yang, and Y. Zhou conceived the structure of this perspective. W. Gao, H. N. Li, and J. Q. Hu prepared the draft. Y. J. Xiong, J. H. Ye, and Z. G. Zou reviewed and refined the manuscript.

## Conflicts of interest

There are no conflicts to declare.

## Acknowledgements

The authors wish to acknowledge the support of the National Key R&D Program of China (2018YFE0208500 and 2021YFA1500700), the NSF of China (21972065 and 22202152), the NSF of Jiangsu Province (No. BK20220006), the Hefei National Laboratory for Physical Sciences at the Microscale (KF2020006), the Program for Guangdong Introducing Innovative and Entrepreneurial Team (2019ZL08L101) and the University Development Fund (UDF01001159).

## References

- 1 C. Y. Feng, Z. P. Wu, K. W. Huang, J. H. Ye and H. B. Zhang, *Adv. Mater.*, 2022, **34**, 202200180.
- 2 E. Gong, S. Ali, C. B. Hiragond, H. S. Kim, N. S. Powar, D. Kim, H. Kim and S. I. In, *Energy Environ. Sci.*, 2022, **15**, 880–937.





- 3 H. W. Lin, S. N. Luo, H. B. Zhang and J. H. Ye, *Joule*, 2022, **6**, 294–314.
- 4 R. Ham, C. J. Nielsen, S. Pullen and J. N. H. Reek, *Chem. Rev.*, 2023, **123**, 5225–5261.
- 5 X. J. Liu, T. Q. Chen, Y. H. Xue, J. C. Fan, S. L. Shen, M. Hossain, M. A. Amin, L. K. Pan, X. T. Xu and Y. Yamauchi, *Coord. Chem. Rev.*, 2022, **459**, 214440.
- 6 B. C. Qiu, M. M. Du, Y. X. Ma, Q. H. Zhu, M. Y. Xing and J. L. Zhang, *Energy Environ. Sci.*, 2021, **14**, 5260–5288.
- 7 K. H. Chen, X. W. Wang, Q. Y. Li, Y. N. Feng, F. F. Chen and Y. Yu, *Chem. Eng. J.*, 2021, **418**, 129476.
- 8 L. Cheng, D. N. Zhang, Y. L. Liao, J. J. Fan and Q. J. Xiang, *Chin. J. Catal.*, 2021, **42**, 131–140.
- 9 J. W. Jiang, X. F. Wang, Q. J. Xu, Z. Y. Mei, L. Y. Duan and H. Guo, *Appl. Catal., B*, 2022, **316**, 121679.
- 10 G. H. Li, Y. Y. Sun, Q. M. Zhang, Z. Gao, W. Sun and X. X. Zhou, *Chem. Eng. J.*, 2021, **410**, 128397.
- 11 J. X. Liang, H. Yu, J. J. Shi, B. Li, L. X. Wu and M. Wang, *Adv. Mater.*, 2023, **35**, 202209814.
- 12 W. B. Jiang, H. Y. Loh, B. Q. L. Low, H. J. Zhu, J. X. Low, J. Z. X. Heng, K. Y. Tang, Z. B. Li, X. J. Loh, E. Y. Ye and Y. J. Xiong, *Appl. Catal., B*, 2023, **321**, 122079.
- 13 S. M. Mao, J. W. Shi, G. T. Sun, D. D. Ma, C. He, Z. X. Pu, K. L. Song and Y. H. Cheng, *Appl. Catal., B*, 2021, **282**, 119550.
- 14 Z. Y. Dong, L. Zhang, J. Gong and Q. Zhao, *Chem. Eng. J.*, 2021, **403**, 126383.
- 15 S. K. Yin, L. L. Sun, Y. J. Zhou, X. Li, J. Z. Li, X. H. Song, P. W. Huo, H. Q. Wang and Y. S. Yan, *Chem. Eng. J.*, 2021, **406**, 126776.
- 16 J. Zhang, L. T. Li, M. Du, Y. Cui, Y. H. Li, W. Yan, H. J. Huang, X. A. Li and X. B. Zhu, *Small*, 2023, **19**, 202300402.
- 17 H. H. Ou, S. B. Ning, P. Zhu, S. H. Chen, A. Han, Q. Kang, Z. F. Hu, J. H. Ye, D. S. Wang and Y. D. Li, *Angew. Chem., Int. Ed.*, 2022, **61**, 202206579.
- 18 J. P. Sheng, Y. He, J. Y. Li, C. W. Yuan, H. W. Huang, S. Y. Wang, Y. J. Sun, Z. M. Wang and F. Dong, *ACS Nano*, 2020, **14**, 13103–13114.
- 19 N. Podrojková, V. Sans, A. Orinak and R. Orinaková, *ChemCatChem*, 2020, **12**, 1802–1825.
- 20 J. Wang, W. B. Zhu, F. Y. Meng, G. Y. Bai, Q. F. Zhang and X. W. Lan, *ACS Catal.*, 2023, **13**, 4316–4329.
- 21 F. F. Chen, L. H. Zhou, C. Peng, D. T. Zhang, L. Y. Li, D. F. Xue and Y. Yu, *Appl. Catal., B*, 2023, **331**, 122689.
- 22 J. Di, C. Chen, C. Zhu, P. Song, M. L. Duan, J. Xiong, R. Long, M. Z. Xu, L. X. Kang, S. S. Guo, S. M. Chen, H. L. Chen, Z. Chi, Y. X. Weng, H. M. Li, L. Song, M. H. Wu, Q. Y. Yan, S. Z. Li and Z. Liu, *Nano Energy*, 2021, **79**, 105429.
- 23 J. Li, B. J. Huang, Q. Guo, S. Guo, Z. K. Peng, J. Liu, Q. Y. Tian, Y. P. Yang, Q. Xu, Z. Y. Liu and B. Liu, *Appl. Catal., B*, 2021, **284**, 119733.
- 24 H. W. Guo, S. P. Wan, Y. A. Wang, W. H. Ma, Q. Zhong and J. Ding, *Chem. Eng. J.*, 2021, **412**, 128646.
- 25 J. Li, W. F. Pan, Q. Y. Liu, Z. Q. Chen, Z. J. Chen, X. Z. Feng and H. Chen, *J. Am. Chem. Soc.*, 2021, **143**, 6551–6559.
- 26 Y. Y. Wang, H. L. Huang, Z. Z. Zhang, C. Wang, Y. Y. Yang, Q. Li and D. S. Xu, *Appl. Catal., B*, 2021, **282**, 119570.
- 27 L. Cheng, P. Zhang, Q. Y. Wen, J. J. Fan and Q. J. Xiang, *Chin. J. Catal.*, 2022, **43**, 451–460.
- 28 Q. J. Wu, J. Liang, Y. B. Huang and R. Cao, *Acc. Chem. Res.*, 2022, **55**, 2978–2997.
- 29 F. Guo, R. X. Li, S. Z. Yang, X. Y. Zhang, H. J. Yu, J. J. Urban and W. Y. Sun, *Angew. Chem., Int. Ed.*, 2023, **62**, 202216232.
- 30 W. Wang, C. Y. Deng, S. J. Xie, Y. F. Li, W. Y. Zhang, H. Sheng, C. C. Chen and J. C. Zhao, *J. Am. Chem. Soc.*, 2021, **143**, 2984–2993.
- 31 G. Wang, Z. Chen, T. Wang, D. S. Wang and J. J. Mao, *Angew. Chem., Int. Ed.*, 2022, **61**, 202210789.
- 32 X. H. Yang, X. W. Lan, Y. Z. Zhang, H. S. Li and G. Y. Bai, *Appl. Catal., B*, 2023, **325**, 122393.
- 33 H. Yu, C. Sun, Y. Xuan, K. Zhang and K. Chang, *Chem. Eng. J.*, 2022, **430**, 132940.
- 34 S. P. Wan, M. Ou, Q. Zhong and X. M. Wang, *Chem. Eng. J.*, 2019, **358**, 1287–1295.
- 35 S. L. Wang, M. Xu, T. Y. Peng, C. X. Zhang, T. Li, I. Hussain, J. Y. Wang and B. E. Tan, *Nat. Commun.*, 2019, **10**, 08651.
- 36 G. Wang, R. Huang, J. W. Zhang, J. J. Mao, D. S. Wang and Y. D. Li, *Adv. Mater.*, 2021, **33**, 202105904.
- 37 X. L. Zhuang, S. T. Zhang, Y. J. Tang, F. Yu, Z. M. Li and H. Pang, *Coord. Chem. Rev.*, 2023, **490**, 215208.
- 38 T. Wang, L. Chen, C. Chen, M. T. Huang, Y. J. Huang, S. J. Liu and B. X. Li, *ACS Nano*, 2022, **16**, 2306–2318.
- 39 P. Y. Li, L. Liu, W. J. An, H. Wang, H. X. Guo, Y. H. Liang and W. Q. Cui, *Appl. Catal., B*, 2020, **266**, 118618.
- 40 Y. J. Liang, X. Wu, X. Y. Liu, C. H. Li and S. W. Liu, *Appl. Catal., B*, 2022, **304**, 120978.
- 41 S. J. Xie, W. C. Ma, X. J. Wu, H. K. Zhang, Q. H. Zhang, Y. D. Wang and Y. Wang, *Energy Environ. Sci.*, 2021, **14**, 37–89.
- 42 Y. N. Teja and M. Sakar, *Small*, 2023, **19**, 202303980.
- 43 W. G. Tu, Y. Zhou, Q. Liu, Z. P. Tian, J. Gao, X. Y. Chen, H. T. Zhang, J. G. Liu and Z. G. Zou, *Adv. Funct. Mater.*, 2012, **22**, 1215–1221.
- 44 X. H. Yan, J. J. Zhang, G. Z. Hao, W. Jiang and J. Di, *Small*, 2024, **20**, 202306742.
- 45 Y. M. Zhou, Q. X. Zhang, X. L. Shi, Q. Song, C. J. Zhou and D. L. Jiang, *J. Colloid Interface Sci.*, 2022, **608**, 2809–2819.
- 46 Y. Shen, C. J. Ren, L. R. Zheng, X. Y. Xu, R. Long, W. Q. Zhang, Y. Yang, Y. C. Zhang, Y. F. Yao, H. Q. Chi, J. L. Wang, Q. Shen, Y. J. Xiong, Z. G. Zou and Y. Zhou, *Nat. Commun.*, 2023, **14**, 1117.
- 47 L. J. Xiong, Y. J. Hu, Y. Wang, W. Dong, X. Y. Zhang, K. Zhang, T. Y. Wang, J. Y. Shen and Y. Yang, *Appl. Catal., B*, 2024, **340**, 123263.
- 48 H. Pang, X. G. Meng, H. Song, W. Zhou, G. L. Yang, H. W. Zhang, Y. Izumi, T. Takei, W. Jewaswan, N. Fukata and J. H. Ye, *Appl. Catal., B*, 2019, **244**, 1013–1020.
- 49 X. D. Zhang, D. Kim and L. Y. S. Lee, *ACS Appl. Energy Mater.*, 2021, **4**, 2586–2592.
- 50 C. Hu, H. Y. Sun, X. M. Jia, H. L. Lin, J. Cao and S. F. Chen, *ChemPhotoChem*, 2022, **6**, 202200150.





- 51 Y. Q. He, C. L. Chen, Y. X. Liu, Y. L. Yang, C. G. Li, Z. Shi, Y. Han and S. H. Feng, *Nano Lett.*, 2022, **22**, 4970–4978.
- 52 S. Si, H. Shou, Y. Mao, X. Bao, G. Zhai, K. Song, Z. Wang, P. Wang, Y. Liu, Z. Zheng, Y. Dai, L. Song, B. Huang and H. Cheng, *Angew. Chem., Int. Ed.*, 2022, **61**, e202209446.
- 53 Y. Q. He, H. Rao, K. P. Song, J. X. Li, Y. Yu, Y. Lou, C. G. Li, Y. Han, Z. Shi and S. H. Feng, *Adv. Funct. Mater.*, 2019, **29**, 201905153.
- 54 W. Gao, S. Li, H. C. He, X. N. Li, Z. X. Cheng, Y. Yang, J. L. Wang, Q. Shen, X. Y. Wang, Y. J. Xiong, Y. Zhou and Z. G. Zou, *Nat. Commun.*, 2021, **12**, 4747.
- 55 W. Gao, L. Shi, W. Hou, C. Ding, Q. Liu, R. Long, H. Chi, Y. Zhang, X. Xu, X. Ma, Z. Tang, Y. Yang, X. Wang, Q. Shen, Y. Xiong, J. Wang, Z. Zou and Y. Zhou, *Angew. Chem., Int. Ed.*, 2024, **63**, e202317852.
- 56 X. Y. Xiong, Y. F. Zhao, R. Shi, W. J. Yin, Y. X. Zhao, G. I. N. Waterhouse and T. R. Zhang, *Sci. Bull.*, 2020, **65**, 987–994.
- 57 S. Yu, L. Tan, S. Bai, C. J. Ning, G. H. Liu, H. J. Wang, B. Liu, Y. F. Zhao and Y. F. Song, *Small*, 2022, **18**, 202202334.
- 58 Y. L. Li, Q. Zhao, X. J. Liu, Y. Liu, Y. J. Hao, X. J. Wang, X. Y. Liu, D. Hildebrandt, F. Y. Li and F. T. Li, *Small Struct.*, 2023, **4**, 202300177.
- 59 Z. H. Wei, S. J. Song, H. F. Gu, Y. Q. Li, Q. Sun, N. Ding, H. Tang, L. R. Zheng, S. H. Liu, Z. X. Li, W. X. Chen, S. H. Li and S. P. Pang, *Adv. Sci.*, 2023, **10**, 202303206.
- 60 K. Sun, Y. Qian and H. L. Jiang, *Angew. Chem., Int. Ed.*, 2023, **62**, e202217565.
- 61 J. X. Wang, K. Sun, D. A. Wang, X. W. Niu, Z. Y. Lin, S. Y. Wang, W. J. Yang, J. R. Huang and H. L. Jiang, *ACS Catal.*, 2023, **13**, 8760–8769.
- 62 M. R. Zhang, D. Zhang, X. Jing, B. J. Xu and C. Y. Duan, *Angew. Chem., Int. Ed.*, 2024, **63**, 202402755.
- 63 Y. Z. Zhang, L. L. Cao, G. Y. Bai and X. W. Lan, *Small*, 2023, **19**, 202300035.
- 64 W. G. Tu, Y. Q. Yang, C. P. Chen, T. H. Zhou, T. H. Li, H. J. Wang, S. Y. Wu, Y. Zhou, D. O'Hare, Z. G. Zou and R. Xu, *Small Struct.*, 2023, **4**, 202200233.
- 65 Q. Zhang, S. Q. Gao, Y. Y. Guo, H. Y. Wang, J. S. Wei, X. F. Su, H. C. Zhang, Z. M. Liu and J. J. Wang, *Nat. Commun.*, 2023, **14**, 1147.
- 66 M. P. Kou, W. Liu, Y. Y. Wang, J. D. Huang, Y. L. Chen, Y. Zhou, Y. Chen, M. Z. Ma, K. Lei, H. Q. Xie, P. K. Wong and L. Q. Ye, *Appl. Catal., B*, 2021, **291**, 120146.
- 67 P. Chen, B. Lei, X. A. Dong, H. Wang, J. P. Sheng, W. Cui, J. Y. Li, Y. J. Sun, Z. M. Wang and F. Dong, *ACS Nano*, 2020, **14**, 15841–15852.
- 68 K. Wang, M. Cheng, F. J. Xia, N. Cao, F. X. Zhang, W. K. Ni, X. Y. Yue, K. P. Yan, Y. He, Y. Shi, W. X. Dai and P. F. Xie, *Small*, 2023, **19**, 202207581.
- 69 L. Cheng, X. Y. Yue, L. X. Wang, D. N. Zhang, P. Zhang, J. J. Fan and Q. J. Xiang, *Adv. Mater.*, 2021, **33**, 202105135.
- 70 L. Zeng, J. W. Chen, L. X. Zhong, W. L. Zhen, Y. Y. Tay, S. Z. Li, Y. G. Wang, L. M. Huang and C. Xue, *Appl. Catal., B*, 2022, **307**, 121154.
- 71 W. Xia and F. Wang, *Mol. Catal.*, 2023, **535**, 112884.
- 72 Y. C. Wang, J. H. Zhang, W. Yang, W. X. Tao, K. Y. Tao, J. H. Deng, W. J. Shi, D. C. Zhong and T. B. Lu, *Chin. J. Chem.*, 2023, **41**, 3305–3310.
- 73 L. Yuan, L. Zhang, X. X. Li, J. Liu, J. J. Liu, L. Z. Dong, D. S. Li, S. L. Li and Y. Q. Lan, *Chin. Chem. Lett.*, 2023, **34**, 039.
- 74 R. Xu, D. H. Si, S. S. Zhao, Q. J. Wu, X. S. Wang, T. F. Liu, H. Zhao, R. Cao and Y. B. Huang, *J. Am. Chem. Soc.*, 2023, **145**, 8261–8270.
- 75 J. Q. Ning, W. Chen, Q. Niu, L. Y. Li and Y. Yu, *ChemSusChem*, 2024, DOI: [10.1002/cssc.202301963](https://doi.org/10.1002/cssc.202301963).
- 76 S. J. Liang, X. H. Zhong, Z. Q. Zhong, H. Deng and W. Y. Wong, *Appl. Catal., B*, 2023, **337**, 122958.
- 77 H. B. Yin, F. Dong, D. S. Wang and J. H. Li, *ACS Catal.*, 2022, **12**, 14096–14105.
- 78 C. Y. Shen, X. Y. Meng, R. Zou, K. H. Sun, Q. L. Wu, Y. X. Pan and C. J. Liu, *Angew. Chem., Int. Ed.*, 2024, **63**, 202402369.
- 79 Q. Y. Wang, Y. D. Zhang, M. X. Lin, H. W. Wang, Y. Bai, C. Y. Liu, J. L. Lu, Q. Q. Luo, G. M. Wang, H. L. Jiang, T. Yao and X. S. Zheng, *Adv. Energy Mater.*, 2023, **13**, 202302692.
- 80 F. Guo, R. X. Li, S. Yang, X. Y. Zhang, H. Yu, J. J. Urban and W. Y. Sun, *Angew. Chem., Int. Ed.*, 2023, **62**, 202216232.
- 81 H. Shi, Y. Liang, J. Hou, H. Wang, Z. Jia, J. Wu, F. Song, H. Yang and X. Guo, *Angew. Chem., Int. Ed.*, 2024, **63**, e202404884.
- 82 Y. Y. Mao, M. H. Zhang, S. H. Si, G. Y. Zhai, X. L. Bao, K. P. Song, L. R. Zheng, Y. Y. Liu, Z. Y. Wang, Z. K. Zheng, P. Wang, Y. Dai, H. F. Cheng and B. B. Huang, *ACS Catal.*, 2023, **13**, 8362–8371.
- 83 C. Y. Feng, T. T. Bo, P. Maity, S. W. Zuo, W. Zhou, K. W. Huang, O. F. Mohammed and H. B. Zhang, *Adv. Funct. Mater.*, 2023, **34**, 202309761.
- 84 C. Ding, X. X. Lu, B. Tao, L. Q. Yang, X. Y. Xu, L. Q. Tang, H. Q. Chi, Y. Yang, D. M. Meira, L. Wang, X. Zhu, S. Li, Y. Zhou and Z. G. Zou, *Adv. Funct. Mater.*, 2023, **33**, 202302824.
- 85 W. K. Xie, K. J. Li, X. H. Liu, X. Zhang and H. W. Huang, *Adv. Mater.*, 2023, **35**, 202208132.
- 86 F. H. Zhou, Y. L. Zhang, J. Wu, W. Yang, X. Fang, T. Jia, Y. Ling, P. He, Q. Z. Liu and J. Lin, *Appl. Catal., B*, 2024, **341**, 123347.
- 87 X. Sun, L. Sun, G. Li, Y. Tuo, C. Ye, J. Yang, J. Low, X. Yu, J. H. Bitter, Y. Lei, D. Wang and Y. Li, *Angew. Chem., Int. Ed.*, 2022, **61**, 202207677.
- 88 S. Hu, P. Z. Qiao, X. L. Yi, Y. M. Lei, H. L. Hu, J. H. Ye and D. F. Wang, *Angew. Chem., Int. Ed.*, 2023, **62**, 202304585.
- 89 M. Z. Ma, Z. Huang, L. A. Li, W. D. Zhang, R. Guo, R. Y. Zhang, W. Fa, C. Q. Han, Y. H. Cao, S. Yu and Y. Zhou, *Appl. Catal., B*, 2023, **330**, 122626.
- 90 J. Zhou, J. Li, L. Kan, L. Zhang, Q. Huang, Y. Yan, Y. F. Chen, J. Liu, S. L. Li and Y. Q. Lan, *Nat. Commun.*, 2022, **13**, 32449.
- 91 M. Zhou, Z. Q. Wang, A. H. Mei, Z. F. Yang, W. Chen, S. Y. Ou, S. Y. Wang, K. Q. Chen, P. Reiss, K. Qi, J. Y. Ma and Y. L. Liu, *Nat. Commun.*, 2023, **14**, 2473.
- 92 X. D. Li, Y. F. Sun, J. Q. Xu, Y. J. Shao, J. Wu, X. L. Xu, Y. Pan, H. X. Ju, J. F. Zhu and Y. Xie, *Nat. Energy*, 2019, **4**, 690–699.



- 93 S. M. Deng, R. H. Wang, X. Z. Feng, R. J. Zheng, S. K. Gong, X. H. Chen, Y. Z. Shangguan, L. L. Deng, H. Tang, H. Dai, L. L. Duan, C. Y. Liu, Y. Pan and H. Chen, *Angew. Chem., Int. Ed.*, 2023, **62**, 202309625.
- 94 C. Chen, L. Chen, Y. G. Hu, K. Yan, T. Wang, Y. J. Huang, C. Gao, J. J. Mao, S. J. Liu and B. X. Li, *J. Energy Chem.*, 2023, **86**, 599–608.
- 95 Y. Z. Zhang, B. Johannessen, P. Zhang, J. L. Gong, J. R. Ran and S. Z. Qiao, *Adv. Mater.*, 2023, **35**, 202306923.
- 96 J. C. Zhu, W. W. Shao, X. D. Li, X. C. Jiao, J. F. Zhu, Y. F. Sun and Y. Xie, *J. Am. Chem. Soc.*, 2021, **143**, 18233–18241.
- 97 J. X. Ji, R. R. Li, H. Zhang, Y. N. Duan, Q. Liu, H. Z. Wang and Z. R. Shen, *Appl. Catal., B*, 2023, **321**, 122020.
- 98 H. Shi, H. Wang, Y. Zhou, J. Li, P. Zhai, X. Li, G. G. Gurzadyan, J. Hou, H. Yang and X. Guo, *Angew. Chem., Int. Ed.*, 2022, **61**, 202208904.
- 99 B. Liu, M. Cheng, C. Zhang, Y. Si, J. Zhou, Y. Ren, J. Guan, L. Duan, M. Liu, D. Jing and N. Li, *Appl. Catal., B*, 2024, **357**, 124263.
- 100 X. F. Shang, G. J. Li, R. A. Wang, T. Xie, J. Ding and Q. Zhong, *Chem. Eng. J.*, 2023, **456**, 140805.
- 101 G. R. Jia, M. Z. Sun, Y. Wang, Y. B. Shi, L. Z. Zhang, X. Q. Cui, B. L. Huang and J. C. Yu, *Adv. Funct. Mater.*, 2022, **32**, 202206817.
- 102 J. L. Yin, D. Y. Li, C. Sun, Y. L. Jiang, Y. K. Li and H. H. Fei, *Adv. Mater.*, 2024, **36**, 2403651.
- 103 W. W. Wang, S. J. Song, P. Wang, M. He, Z. Fang, X. L. Yuan, H. Li, C. Y. Li, X. Wang, Y. C. Wei, W. Y. Song, H. Xu and Z. X. Li, *ACS Catal.*, 2023, **13**, 4597–4610.
- 104 S. J. Xie, Y. F. Li, B. Sheng, W. Y. Zhang, W. Wang, C. C. Chen, J. K. Li, H. Sheng and J. C. Zhao, *Appl. Catal., B*, 2022, **310**, 121320.
- 105 Z. F. Ma, X. Liu, X. S. Wang, Z. G. Luo, W. R. Li, Y. H. Nie, L. Pei, Q. A. Mao, X. Wen and J. S. Zhong, *Chem. Eng. J.*, 2023, **468**, 143569.
- 106 Y. Y. Duan, Y. Wang, W. X. Zhang, J. W. Zhang, C. G. Ban, D. M. Yu, K. Zhou, J. J. Tang, X. Zhang, X. D. Han, L. Y. Gan, X. P. Tao and X. Y. Zhou, *Adv. Funct. Mater.*, 2023, **33**, 202301729.
- 107 J. Y. Wang, C. Yang, L. Mao, X. Y. Cai, Z. K. Geng, H. Y. Zhang, J. Y. Zhang, X. Tan, J. H. Ye and T. Yu, *Adv. Funct. Mater.*, 2023, **33**, 202213901.
- 108 X. Shi, W. D. Dai, X. A. Dong, Q. Ren, J. P. Sheng and F. Dong, *Appl. Catal., B*, 2023, **339**, 123147.
- 109 W. G. Pan, C. F. Li, Z. R. Zhang, T. Wu and R. T. Guo, *Appl. Catal., B*, 2024, **343**, 123492.
- 110 A. X. Deng, E. Zhao, Q. Li, Y. Sun, Y. Z. Liu, S. G. Yang, H. He, Y. Xu, W. Zhao, H. O. Song, Z. Xu and Z. P. Chen, *ACS Nano*, 2023, **17**, 11869–11881.
- 111 M. H. Zhang, Y. Y. Mao, X. L. Bao, P. Wang, Y. Y. Liu, Z. K. Zheng, H. F. Cheng, Y. Dai, Z. Y. Wang and B. B. Huang, *ACS Catal.*, 2024, **14**, 5275–5285.
- 112 P. G. Liu, Z. X. Huang, X. P. Gao, X. Hong, J. F. Zhu, G. M. Wang, Y. E. Wu, J. Zeng and X. S. Zheng, *Adv. Mater.*, 2022, **34**, 202200057.
- 113 X. H. Li, F. H. Li, S. L. Tong, Y. J. Cao, Y. W. Jiang, Z. M. Wang, W. Lu, J. Wu, T. Zhou, J. Lin and Y. S. Liu, *J. Alloys Compd.*, 2024, **984**, 173986.
- 114 X. T. Wang, Z. Z. Wang, Y. Li, J. T. Wang and G. K. Zhang, *Appl. Catal., B*, 2022, **319**, 121895.
- 115 Y. Zhang, F. Y. Guo, K. K. Wang, J. Di, B. K. Min, H. Y. Zhu, H. L. Chen, Y. X. Weng, J. Y. Dai, Y. B. She, J. X. Xia and H. M. Li, *Chem. Eng. J.*, 2023, **465**, 142663.
- 116 G. Wang, Y. Wu, Z. Li, Z. Lou, Q. Chen, Y. Li, D. Wang and J. Mao, *Angew. Chem., Int. Ed.*, 2023, **62**, e202218460.
- 117 Z. W. Zhao, Z. L. Wang, J. F. Zhang, C. F. Shao, K. Dai, K. Fan and C. H. Liang, *Adv. Funct. Mater.*, 2023, **33**, 202214470.
- 118 H. A. E. Omr, R. Putikam, S. P. Feng, M. C. Lin and H. Lee, *Appl. Catal., B*, 2023, **339**, 123103.
- 119 C. J. Ning, J. R. Yang, S. Bai, G. B. Chen, G. H. Liu, T. Y. Shen, L. R. Zheng, S. M. Xu, X. G. Kong, B. Liu, Y. F. Zhao and Y. F. Song, *Adv. Funct. Mater.*, 2023, **33**, 202300365.
- 120 S. Q. Gong, Y. L. Niu, X. Liu, C. Xu, C. C. Chen, T. J. Meyer and Z. F. Chen, *ACS Nano*, 2023, **17**, 4922–4932.
- 121 Y. Zhao, Z. D. Han, G. Y. Gao, W. Y. Zhang, Y. Qu, H. Y. Zhu, P. F. Zhu and G. F. Wang, *Adv. Funct. Mater.*, 2021, **31**, 202104976.
- 122 W. L. Dai, P. Wang, J. F. Long, Y. Xu, M. Zhang, L. X. Yang, J. P. Zou, X. B. Luo and S. L. Luo, *ACS Catal.*, 2023, **13**, 2513–2522.
- 123 H. B. Zhao, J. N. Huang, Q. Qin, H. Y. Chen and D. B. Kuang, *Small*, 2023, **19**, 202302022.
- 124 M. L. Guan, N. Lu, X. Zhang, Q. W. Wang, J. Bao, G. Y. Chen, H. Yu, H. M. Li, J. X. Xia and X. Z. Gong, *Carbon Energy*, 2023, **6**, e420.
- 125 H. J. Lu, N. Uddin, Z. H. Sun, Z. B. Chen, Z. Mahfoud, Y. L. Wu, A. A. Wibowo, Z. C. Su, X. M. Yin, C. S. Tang, X. Z. Liao, S. P. Ringer, X. S. Zhao, A. T. S. Wee, M. Bosman and Z. Y. Yin, *Nano Energy*, 2023, **115**, 108684.
- 126 X. Y. Jiang, J. D. Huang, Z. H. Bi, W. J. Ni, G. Gurzadyan, Y. A. Zhu and Z. Y. Zhang, *Adv. Mater.*, 2022, **34**, 202109330.
- 127 D. Li, C. J. Zhou, X. L. Shi, Q. Zhang, Q. Song, Y. M. Zhou and D. L. Jiang, *Appl. Surf. Sci.*, 2022, **598**, 153843.
- 128 J. Y. Wang, Y. Z. Li, J. T. Zhao, Z. Xiong, Y. C. Zhao and J. Y. Zhang, *Catal. Sci. Technol.*, 2022, **12**, 3454–3463.
- 129 Y. Y. Yu, Y. He, P. Yan, S. Y. Wang and F. Dong, *Proc. Natl. Acad. Sci. U. S. A.*, 2023, **120**, 2307320120.
- 130 B. W. Zhou, Y. J. Ma, P. F. Ou, Z. W. Ye, X. Y. Li, S. Vanka, T. Ma, H. D. Sun, P. Wang, P. Zhou, J. K. Cooper, Y. X. Xiao, I. A. Navid, J. Pan, J. Song and Z. T. Mi, *Nat. Catal.*, 2023, **6**, 987–995.
- 131 N. Y. Huang, B. Li, D. J. Wu, Z. Y. Chen, B. Shao, D. Chen, Y. T. Zheng, W. J. Wang, C. Z. Yang, M. Gu, L. Li and Q. Xu, *Angew. Chem., Int. Ed.*, 2024, **63**, e202319177.
- 132 D. W. Zhao, Y. M. Xuan, K. Zhang and X. L. Liu, *ChemSusChem*, 2021, **14**, 3293–3302.
- 133 W. Lyu, Y. Liu, J. Y. Zhou, D. T. Chen, X. Zhao, R. Q. Fang, F. L. Wang and Y. W. Li, *Angew. Chem., Int. Ed.*, 2023, **62**, 202310733.



- 134 Y. Zhang, H. L. Shi, S. Y. Zhao, Z. L. Chen, Y. Y. Zheng, G. M. Tu, S. X. Zhong, Y. L. Zhao and S. Bai, *Small*, 2024, **20**, 202304050.
- 135 Y. X. Miao, Y. X. Zhao, S. Zhang, R. Shi and T. R. Zhang, *Adv. Mater.*, 2022, **34**, 202200868.
- 136 C. L. Tan, M. Y. Qi, Z. R. Tang and Y. J. Xu, *ACS Catal.*, 2023, **13**, 8317–8329.
- 137 S. P. Mo, X. Y. Zhao, S. D. Li, L. L. Huang, X. Zhao, Q. M. Ren, M. Y. Zhang, R. S. Peng, Y. A. Zhang, X. B. Zhou, Y. M. Fan, Q. L. Xie, Y. B. Guo, D. Q. Ye and Y. F. Chen, *Angew. Chem., Int. Ed.*, 2023, **62**, 202313868.
- 138 G. P. Zhang, X. X. Li, D. Y. Chen, N. J. Li, Q. F. Xu, H. Li and J. M. Lu, *Adv. Funct. Mater.*, 2023, **33**, 202308553.
- 139 R. Z. Chen, S. H. Chen, L. Q. Wang and D. S. Wang, *Adv. Mater.*, 2023, **36**, 202304713.
- 140 M. Jung, C. W. Kim, S. Y. Kim, A. U. Pawar, D. K. Lee and Y. S. Kang, *Adv. Energy Mater.*, 2022, **12**, 202202160.
- 141 C. W. Kim, Y. S. Son, M. J. Kang, D. Y. Kim and Y. S. Kang, *Adv. Energy Mater.*, 2016, **6**, 201501754.
- 142 C. W. Kim, S. J. Yeob, H. M. Cheng and Y. S. Kang, *Energy Environ. Sci.*, 2015, **8**, 3646–3653.
- 143 A. U. Pawar, C. W. Kim, M. J. Kang and Y. S. Kang, *Nano Energy*, 2016, **20**, 156–167.
- 144 C. W. Kim, A. U. Pawar, T. Hawari, N. H. Ahn, D. K. Lee, L. Yang, R. P. Sivasankaran, J. Tang, Z. B. Zhuo and Y. S. Kang, *Sci. Rep.*, 2022, **12**, 20045–20046.
- 145 A. U. Pawar, U. Pal, J. Y. Zheng, C. W. Kim and Y. S. Kang, *Appl. Catal., B*, 2022, **303**, 120921.
- 146 L. A. Li, Z. C. Chai, W. Jin, H. Sun, J. H. He, G. Q. Wu and W. W. Xia, *J. Alloys Compd.*, 2023, **932**, 167658.

